

Complete and Near-Optimal Robotic Crack Coverage and Filling in Civil Infrastructure

Vishnu Veeraraghavan, Kyle Hunte, Jingang Yi, and Kaiyan Yu

Abstract—We present a simultaneous sensor-based inspection and footprint coverage (SIFC) planning and control design with applications to autonomous robotic crack mapping and filling. The main challenge of the SIFC problem lies in the coupling of complete sensing (for mapping) and robotic footprint (for filling) coverage tasks. Initially, we assume known target information (e.g., crack) and employ classic cell decomposition methods to achieve complete sensing coverage of the workspace and complete robotic footprint coverage using the least-cost route. Subsequently, we generalize the algorithm to handle unknown target information, allowing the robot to scan and incrementally construct the target graph online while conducting robotic footprint coverage. The online polynomial-time SIFC planning algorithm minimizes the total robot traveling distance, guarantees complete sensing coverage of the entire workspace, and achieves near-optimal robotic footprint coverage, as demonstrated through empirical experiments. For the demonstrated application, we design coordinated nozzle motion control with the planned robot trajectory to efficiently fill all cracks within the robot’s footprint. Experimental results are presented to illustrate the algorithm’s design, performance, and comparisons. The SIFC algorithm offers a high-efficiency motion planning solution for various robotic applications requiring simultaneous sensing and actuation coverage.

Index Terms—Coverage planning, construction robots and automation, motion control, Civil infrastructure.

I. INTRODUCTION

Surface cracks commonly exist in civil infrastructure, such as road and bridge deck surfaces, parking lots, airport runways, etc. To prevent crack growth and mitigate further deterioration, it is necessary to fill these cracks with appropriate materials in the early stages of crack appearance. It is labor-intensive, time-consuming, and expensive to repair the abundant existence of cracks in civil infrastructure by human workers. Robotics and automation technologies provide a promising tool to enable cost-effective, safe, and high-efficiency civil infrastructure maintenance. Mobile robot- or vehicle-based inspection systems were used for crack detection and maintenance on highways (e.g., [1], [2]). These systems were not

fully automated, and human inspectors were still involved in operations. The developed autonomous robots in [3]–[5] mainly focused on nondestructive bridge deck inspection and crack mapping and repair were discussed. Crack mapping and filling can be viewed and generalized as a simultaneous robotic sensor-based inspection and footprint coverage (SIFC) problem. The onboard sensing system (e.g., camera) needs to detect all unknown targets (i.e., cracks) in the workspace, and at the same time, the robot must physically cover all the detected targets within its footprint to conduct the repair action. The complexity of the SIFC problem lies in simultaneously achieving the above-mentioned two complete coverage tasks of unknown targets using one robotic platform. The onboard target detection sensing range and the robot footprint have different sizes and geometric shapes. In addition, the robot footprint coverage task (e.g., filling cracks) might involve motion dynamics and control constraints, which is different from the coupled (passive) sensing coverage task. Although inspired by autonomous robotic crack mapping and filling, the SIFC is indeed a fundamental robot motion planning problem in other applications, such as sensing and cleaning dirty surfaces, finding and collecting mines, etc.

The SIFC planning is related to the covering salesman problem, a traveling salesman problem variant in which an agent is required to travel the shortest distance to visit all specified neighborhoods in each city. However, without any knowledge of the locations of each city, the agent must inspect every point in the environment. Other variants include the art gallery problem and the watchman tour problem. However, these problems do not require the footprint coverage of the targets. All of these problems are NP-hard, and therefore, obtaining optimal solutions is only feasible for very limited problem domains [6]. To detect unknown targets, robotic exploration can be applied [7], [8]. In time-critical applications, most exploration paradigms are not efficient due to backtracking, where the robot might return to the same location more than once [9].

Coverage path planning is widely used to explore the unknown environment by determining an optimal path that passes over all points of an area of interest while avoiding obstacles [10], [11]. Based on whether prior environmental information is known or not, coverage path planning methods can be classified into offline or online methods. In offline approaches, known information about the environment is used to produce the shortest or fastest path [12], while in online approaches, sensor information is used to plan coverage motion point-by-point. Many online coverage planning approaches use heuristics to navigate to the nearest cell [13], the cell with

The work was supported in part by the US NSF under award IIS-1426828 (J. Yi). An earlier version of this paper was presented in part at the 2019 IEEE International Conference on Robotics and Automation, Montreal, Canada, May 20–24, 2019 [10.1109/ICRA.2019.8794407]. (*Corresponding author: Kaiyan Yu and Jingang Yi*).

The first two authors equally contributed to the work.

V. Veeraraghavan and K. Yu are with the Department of Mechanical Engineering, Binghamton University, Binghamton, NY 13902 USA (email: vveerar1@binghamton.edu; kyu@binghamton.edu).

K. Hunte and J. Yi are with the Department of Mechanical and Aerospace Engineering, Rutgers University, Piscataway, NJ 08854 USA (email: kdh95@scarletmail.rutgers.edu; jgyi@rutgers.edu).

Videos of the experiments and source codes are available at <https://github.com/Binghamton-ACSR-Lab/Crack-Filling-Robot>.

the highest potential [14], [15], or the cell with the lowest cost [16]. However, as they do not optimize the coverage path from a global perspective, these online planning approaches might fall into the local extremum. When the local extremum occurs, online approaches employ heuristic strategies such as backtracking procedures [17] or potential surfaces [14] to passively identify the next waypoint. These heuristic strategies prevent the robot from getting stuck in the local extremum; however, the robot visits the covered area repeatedly. Alternatively, the coverage path planning approaches in [12], [18] avoided the local extremum by using spanning trees, where the robot was guided to circumvent the virtual tree. These algorithms, however, did not account for partially occupied cells or special tree nodes and therefore resulted in incomplete coverage or repeated coverage [15].

The Morse-based cellular decomposition (MCD) [19] and generalized Boustrophedon decomposition [20] guarantee the complete coverage of an unknown environment. The MCD methods ensure encountering all the critical points of the decomposition online [21]–[23]. Those algorithms perform an online decomposition such that the areas are covered completely by back-and-forth motions. However, no optimality was claimed for the planned paths. The work in [12] proposed an optimal coverage of a known environment. Grid-based approaches for planning a complete coverage path were also studied [24]. But those approaches restricted the space and robot motion to the grids and not to any arbitrary points in the workspace. Readers can further refer to [10], [25] for extensive surveys on coverage-planning strategies.

Online re-planning of the robot’s path is needed when new information is obtained by the onboard sensors [26]. A graph-based Simplex method was presented to solve the re-planning problem [27]. The anytime dynamic A* algorithm is a generic graph-based re-planning scheme that generates bounded sub-optimal solutions when the map changes [28]. Navigation and coverage planning for autonomous underwater vehicles is a closely related problem (e.g., [29]). The existing work, however, focuses only on the unknown environment’s exploration task and does not consider additional simultaneously performing other tasks such as robot footprint coverage. Another piece of closely related work is the efficiently autonomous robotic cleaning or vacuuming [30], [31]. The learned dirt map was used for planning the robot to clean a set of cells. And this is different from the SIFC problem because the initial learning process is costly or infeasible for applications such as the online construction of the crack map for repair. The probabilistic planner in [32] used Monte Carlo localization to achieve complete coverage path planning, but it suffered from accumulating localization errors. Such probabilistic planners can perform online planning in dynamic environments, but they often have a higher computational complexity, rely on certain modeling assumptions (e.g., distributions of obstacles and uncertainty), and provide solutions that are only probabilistic optimal.

In this paper, we present a set of motion planning algorithms for the SIFC with the application of robotic crack-filling in civil infrastructure. Instead of directly solving the SIFC problem, we first discuss the motion planning of a mobile

robot to physically cover the target (i.e., cracks) for a given known target map; that is, no complete sensing coverage is considered. We decouple the two coverage planning tasks using classic cell decomposition methods to achieve complete sensing and robotic footprint coverage of the targets. A near-optimal complete footprint coverage plan is proposed to guide the robot, but with an offline-constructed target graph. The least-cost route is selected to traverse the constructed target graph. Finally, we propose a complete online motion planning solution for the SIFC problem, called the online sensor-based complete coverage (oS_{CC}) algorithm. The oS_{CC} detects unknown targets using onboard sensors when the robot traverses the targets to conduct the filling actuation at the shortest distance. In experiments, the crack-filling robot is equipped with four omni-directional wheels to perform arbitrary direction motion, and an *XY*-table mechanism is used to drive a fluid nozzle to conduct filling action. Motion control of omni-directional-wheel robots was reported in [33], [34]. We formulate motion coordination between the mobile robot and the nozzle movements into a nonlinear model predictive control (MPC). We conducted extensive experiments to validate and demonstrate the proposed planning and control algorithms.

The main contribution of this work is the development of a new, complete, and empirically near-optimal motion planning and control approach for the SIFC problem in robotic crack mapping and filling applications. The proposed planning algorithms offer two key attractive features. Firstly, the novel oS_{CC} algorithm guarantees complete sensing coverage of the free space in the entire workspace while simultaneously achieving complete robotic footprint coverage of the detected targets. This algorithm aims to minimize the total distance traveled by the robot and achieves a near-optimal path in polynomial time. Secondly, the motion control of the robotic filling mechanism is coordinated with the planned mobile robot trajectory, enabling efficient execution of the robot’s footprint task. The coupling between the sensor-based inspection and the onboard footprint coverage actuation is formulated and resolved by a new coordinated robot control design. Compared to the presented conference publications [35], [36], this paper introduces additional analyses for the motion planning and control design. It also presents extensive new experiments and detailed discussions using an upgraded crack-filling robot platform for improved motion planning and control. These developments provide valuable insights and a comprehensive understanding of the proposed approach in various scenarios, enhancing the applicability and reliability of the system.

The rest of the paper is organized as follows: We discuss the problem statement and overview of the planning and control algorithms in Section II. Section III presents the basic footprint coverage planning with known target information. Section IV extends to sensor-based online coverage planning. Section V discusses the robotic control for crack-filling actuation. We present the experimental setup and results in Sections VI and VII, respectively. Finally, we summarize the concluding remarks in Section VIII.

II. PROBLEM STATEMENT AND ALGORITHMS OVERVIEW

A. Problem Statement

Fig. 1 shows an illustrative SIFC setup for the robotic crack-filling application. We consider the coverage planning and motion control for a robot, denoted as \mathbf{R} , which is equipped with a crack detection sensor and filling actuator. \mathbf{R} is in a compact free workspace $\mathcal{W} \subset \mathbb{R}^2$. In general, the free space can be in any shape with a finite number of obstacles. For simplicity, we consider a known rectangular obstacle-free workspace with a size of $l \times w$, and the results are extendable to any other free spaces with different shapes. Readers can refer to [19], [21] for more details. Robot \mathbf{R} needs to completely cover \mathcal{W} to detect all unknown cracks (as targets) and simultaneously fill the detected cracks. \mathbf{R} is assumed to freely move in any arbitrary direction in \mathcal{W} . The robot's footprint, denoted as \mathcal{F} , is a circular area around its geometric center with a radius of a . Any cracks within \mathcal{F} can be repaired by the filling actuator. The onboard target detection sensor (e.g., a panoramic camera) can identify any cracks within a circular area of a radius of S around the robot's geometric center. The target detection range is larger than the robot footprint size, that is, $S \geq a$.

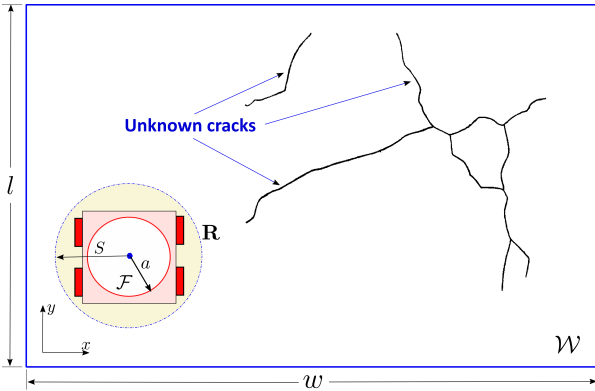


Fig. 1. The illustration of robotic crack inspection and filling setup with unknown crack information in a rectangular workspace \mathcal{W} .

To focus on the coverage planning problem, robot \mathbf{R} is assumed to know its location in \mathcal{W} . Crack widths are assumed constant and \mathbf{R} only needs to consider the crack length as footprint coverage. We also assume that at any time the nozzle-filling motion and the robot motion are coordinated so that any targets under the robot's footprint can be reached by the nozzle. Therefore, we only consider the minimization of the robot's total traveling distance as the goal of the planner.

Problem Statement: Given the unknown targets (e.g., cracks) in \mathcal{W} , the goal of the motion planner and controller for robot \mathbf{R} , with an onboard sensing range S and a robot footprint size a , is to completely detect and footprint-cover all targets in \mathcal{W} while minimizing the total distance traveled by the robot. The objective is to achieve near-optimal solutions, considering the uncertainties associated with the unknown targets. The optimality of the planning algorithm involves finding an efficient path that minimizes the total distance traveled by the robot while covering all the cracks and scanning the entire free space.

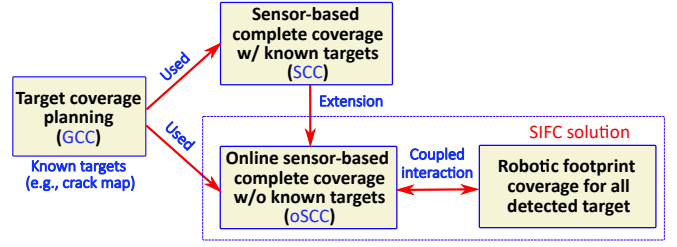


Fig. 2. The overview of the SIFC planning and control algorithms.

B. Algorithm Design Overview

To solve the above SIFC problem, we present a set of algorithmic developments. Fig. 2 illustrates an overview of the planning algorithms and their relationships. First, we describe a robotic coverage planning algorithm, called graph-based coverage (GCC), to drive robot \mathbf{R} to cover all targets by its footprint under a given target map. Note that GCC does not cover the entire workspace \mathcal{W} by using onboard detection sensors, but it serves as a basic planning module to cover the given target map by robotic footprint \mathcal{F} .

We then present a sensor-based complete coverage of workspace \mathcal{W} assuming known target maps, which is denoted as the SCC algorithm. The SCC algorithm initially constructs a graph map from the provided target maps and subsequently utilizes the GCC to explore the entire workspace \mathcal{W} and guide robot \mathbf{R} to achieve footprint coverage of all targets while minimizing travel distance. Serving as the foundation for addressing the SIFC problem, the SCC algorithm plays a crucial role. By leveraging the insights gained from the edge connections observed in the SCC algorithm and its properties of completeness and near-optimality, we extend this approach to handle scenarios with unknown target information, such as unknown cracks. This extension leads to the development of an online SCC algorithm, denoted as oSCC, which is derived from SCC by relaxing the assumption of given target maps to achieve near-optimal sensor-based target detection and real-time robot footprint coverage to completely cover \mathcal{W} . Finally, crack filling control is designed to drive the onboard actuation mechanism to fill the detected targets with coordinated robot motion given by oSCC. Both SCC and oSCC use GCC as part of the algorithmic module. The crack-filling control has to follow the dynamic constraints of the actuator and mechanical systems with the coupled robot motion. The sensor-based detection coverage by the oSCC algorithm and robotic footprint coverage design together provide the SIFC solution. In the next two sections, we present the GCC, SCC, and oSCC algorithms in detail.

III. CRACK COVERAGE PLANNING

In this section, we present the GCC planner for robot footprint coverage of the given target (i.e., crack) map.

A. Target Graph Construction

We construct a target graph, denoted by \mathbb{G}_c , from crack images that are captured by the onboard camera sensors. Because the GCC planner assumes known target maps, as shown in Figs. 1 and 3, the images of the cracks were captured

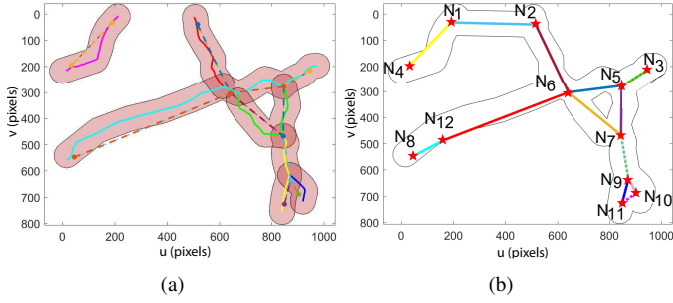


Fig. 3. (a) An example of the footprint region \mathcal{M}_f (red shaded areas). The solid lines are the separated cracks. (b) The constructed \mathbb{G}_c . Points N_1 to N_{12} shown in red stars are nodes of \mathbb{G}_c , and the solid lines are edges of \mathbb{G}_c . The dashed lines are the added edges in the GCC algorithm.

offline using the onboard camera and then stitched together to obtain the entire crack image \mathcal{I} . We first extract the crack skeletons from \mathcal{I} and then dilate the skeletons by circular area with radius a , i.e., Minkowski sum with footprint size. For example, Fig. 3(a) illustrates the dilated skeletons of the cracks shown in Fig. 1. We define the union of all the dilated cracks as *footprint region*, denoted by \mathcal{M}_f . The endpoints (P_{end}) and intersection points (P_{int}) of dilated cracks are used to build the nodes of \mathbb{G}_c , and the crack’s extension directions are used to create the edges of \mathbb{G}_c . Multiple P_{end} and P_{int} are merged if their distances are within a , namely, those points are covered within \mathcal{F} . The edges of \mathbb{G}_c are the shortest distance routes connecting the corresponding nodes inside \mathcal{M}_f . Fig. 3(b) illustrates the example of the constructed graph \mathbb{G}_c .

Algorithm 1 describes the construction of graph \mathbb{G}_c . The input is the binary image \mathcal{I} , which is homography warped according to their actual shape. The first step is to use the skeleton method to find the topology \mathcal{T} of \mathcal{I} (line 1). Endpoints of the cracks, P_{end} , are found from \mathcal{T} by searching the 8 neighbors of each pixel. \mathcal{T} is then separated into individual cracks, $\text{crack}_{\mathcal{I}}$, by the endpoints and crack extension direction (line 2). Lines 3 and 4 find all P_{end} , with a distance larger than a between each other to form end-nodes, N_{end} . Footprint region \mathcal{M}_f is obtained by the Minkowski sum (line 5). The intersected areas A_{int} of all dilations are found, and their corresponding overlapping numbers, N_{over} , and centroid point, P_{int} , are determined (lines 6-7). Among P_{int} and N_{end} being the final candidates for the graph nodes, P_{cand} (line 9), we select the nodes with a distance greater than a with each other as the nodes, \mathbf{N} , of \mathbb{G}_c (line 11). The graph’s edges, \mathbf{E}_c , are obtained from its nodes and crack topology (line 12). Function `shortest_path` is used to adjust the graph edges to guarantee their locations inside the Minkowski area by using visibility graph shortest path planning (line 13)

We need to take special consideration for the different formed angles by cracks. Fig. 4 illustrates a few examples of \mathbb{G}_c with different formed angles. Fig. 4(a) shows a general case where two vertex points (i.e., N_1 and N_2) are far away with a distance larger than a . When a vertex point on \mathcal{T} forms an acute angle, it can overlap with its own Minkowski sum area, which makes the nodes visible to each other; see Fig. 4(b). In this case, the shortest path does not transverse the crack, which leads to unfilled cracks. To achieve the shortest crack-

Algorithm 1: Crack_Graph

```

Input :  $\mathcal{I}$ 
Output:  $\mathbb{G}_c$ 
1  $\mathcal{T} \leftarrow \text{topology}(\mathcal{I})$ ,  $P_{\text{end}} \leftarrow \text{get\_endpoint}(\mathcal{T})$ 
2  $\text{crack}_{\mathcal{I}} \leftarrow \text{get\_cracks}(\mathcal{T}, P_{\text{end}})$ 
  for each  $P_{\text{end}} \rightarrow e_i$  do
3    $P_{\text{test}} \leftarrow P_{\text{end}}/e_i$ 
   if  $\text{all}(\text{distance}(e_i, P_{\text{test}})) > a$  then
4      $N_{\text{end}} \leftarrow \text{add\_node}(e_i)$ 
5  $\mathcal{M}_f \leftarrow \text{crack}_{\mathcal{I}} \oplus a$ 
6  $(A_{\text{int}}, N_{\text{over}}) \leftarrow \text{get\_intersection}(\mathcal{M}_f)$ 
7  $P_{\text{int}} \leftarrow \text{centroid}(A_{\text{int}})$ 
8  $(\text{crack}_{\mathcal{I}}, N_{\text{end}}) \leftarrow \text{shorten}(\text{crack}_{\mathcal{I}}, N_{\text{end}})$ 
9  $N_{\text{cand}} \leftarrow \text{combine}(P_{\text{int}}, N_{\text{end}})$ 
10  $N_{\text{cand}} \leftarrow \text{sort}(N_{\text{cand}}, N_{\text{over}})$ 
   for each  $N_{\text{cand}} \rightarrow n_i$  do
11   if  $\text{distance}(n_i, \mathbf{N}) > a$  then
      $\mathbf{N} \leftarrow \text{add\_node}(n_i)$ 
12  $\mathbf{E}_c \leftarrow \text{search\_edge}(\mathbf{N}, \mathcal{T})$ 
13  $\mathbb{G} \leftarrow \{\mathbf{N}, \mathbf{E}_c\}$ ,  $\mathbb{G}_c \leftarrow \text{shortest\_path}(\mathbb{G}, \mathcal{M}_f)$ 

```

filling path, the vertex must be at least a distance of a from the boundary of the Minkowski sum area. These cracks are pre-identified, and their respective Minkowski offset values are adjusted (line 5 in Algorithm 1). Fig. 4(c) shows the Minkowski sum area with the adjusted Minkowski offset value. By doing so, it guarantees that the calculated shortest path covers the entire crack in `shortest_path`.

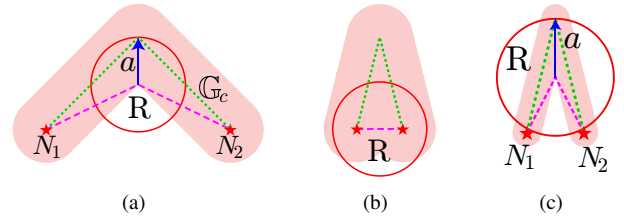


Fig. 4. Illustration of crack graphs with different formed angles. Robot footprint \mathcal{F} is illustrated by a red circle. The graph \mathbb{G}_c is shown as dotted green lines, and the red stars N_1 and N_2 represent its nodes. The pink-shaded areas are the footprint region \mathcal{M}_f . The red dashed lines are the shortest paths to connect nodes N_1 and N_2 within \mathcal{M}_f . (a) Every point on \mathbb{G}_c is covered by \mathcal{F} as robot \mathbf{R} travels along the shortest path. (b) With sharp crack angles, robot \mathbf{R} cannot fully cover \mathbb{G}_c . (c) By adjusting the Minkowski sum area, the shortest path is achieved to ensure full crack coverage.

B. Target Coverage Planning

With \mathbb{G}_c , we consider the required properties of the graph to guide the robot to traverse the cracks with minimum cost. First, all of the graph vertices except the first and last in the route must have an even number of connected edges; otherwise, no route exists in the graph to allow traveling along each edge exactly once; that is, the robot would get stuck at odd vertices. To prevent this, the vertices with an odd number of connected edges are made even by adding edges. To achieve the shortest traveling distance, the robot motion planner must search for all the different means to pair off the vertices with odd numbers

of connected edges and choose the pair that adds the least total distance to the graph.

The task of finding the shortest route covering all the graph edges is similar to the Chinese Postman Problem (CPP) [37]. However, the crack edges might not form a connected graph and instead form subsets of graphs. As a result, when such situations arise, we adapt the rural postman problem (RPP) solution [38]. The RPP was demonstrated to be NP-complete, and heuristic solution procedures were proposed to approximate the solution [39]. Unlike any postman problem in which the postman usually needs to finish at the same location as the starting point, robot \mathbf{R} , however, can start and finish the job at different locations. Therefore, two nodes that have an odd number of connected edges are left unpaired and selected as the starting and ending positions, respectively.

Algorithm 2 illustrates the GCC planning algorithm. The algorithm formulates an RPP problem to guarantee that the robot covers all the cracks with the least number of revisits. The algorithm comprises three phases. In the first phase, the minimum spanning tree is computed over \mathbb{G}_c to get a subset of the edges \mathbb{E}_t that connects all the vertices with the minimum possible total edge weight (line 1). The union of \mathbb{G}_c and \mathbb{E}_t ensures a single connected network for the postman problem. In the second phase, using matching theory [40], we search for all possible ways to pair up the odd vertices, N_{odd} (line 2) by describing the solution as a linear programming (LP) polyhedron. \mathbb{E}_{add} represents the collection of all sets of added edges for every potential pairing, while $\mathbb{E}_{\text{add}}(i)$ indicates the added edge for the i th potential pairing. C_{total} , C_{max} , and C_{final} denote the total, maximum, and final edge cost, respectively. The edge cost is formulated as the line distance. E_{final} is selected as the minimum cost of the total added edges minus the maximum-cost single added edge. The maximum-cost single edge is broken into the starting and ending nodes of the path (lines 3 to 6). The graph is updated by adding E_{final} (line 7). In the final phase, the function `fleury` [41] is used to obtain the optimal path \mathcal{P}_c for \mathbf{R} . For example, as shown in Fig. 3(b), the optimal path is obtained as a sequence $\mathcal{P}_c : N_4 \rightarrow N_1 \rightarrow N_2 \rightarrow N_6 \rightarrow N_5 \rightarrow N_3 \rightarrow N_5 \rightarrow N_7 \rightarrow N_9 \rightarrow N_{10} \rightarrow N_{11} \rightarrow N_9 \rightarrow N_7 \rightarrow N_6 \rightarrow N_{12} \rightarrow N_8$.

Algorithm 2: GCC

Input : \mathbb{G}_c
Output: \mathcal{P}_c

- 1 $\mathbb{E}_t \leftarrow \text{MST}(\mathbb{G}_c)$, $\mathbb{G}_c \leftarrow \mathbb{G}_c \cup \mathbb{E}_t$
- 2 $N_{\text{odd}} \leftarrow \text{find_oddNode}(\mathbb{G}_c)$, $\mathbb{E}_{\text{add}} \leftarrow \text{pair}(N_{\text{odd}}, \mathbb{G}_c)$
for each $\mathbb{E}_{\text{add}} \rightarrow \mathbb{E}_{\text{add}}(i)$ **do**
- 3 $C_{\text{max}} \leftarrow \max(\mathbb{E}_{\text{add}}(i).edgeCost)$
- 4 $C_{\text{total}}(i) \leftarrow \text{sum}(\mathbb{E}_{\text{add}}(i).edgeCost) - C_{\text{max}}$
- 5 $(C_{\text{final}}, \text{Index}) \leftarrow \min(C_{\text{total}})$
- 6 $E_{\text{final}} \leftarrow \mathbb{E}_{\text{add}}(\text{Index}).edge$
- 7 $\mathbb{G}_c \leftarrow \text{add}(\mathbb{G}_c, E_{\text{final}})$, $\mathcal{P}_c \leftarrow \text{fleury}(\mathbb{G}_c)$

Since the distance between any two nodes in \mathbb{G}_c is guaranteed to be at least a , the resulting path \mathcal{P}_c is always less than or equal to the complete coverage of the target map. If

the target map is dense enough, then the graph degrades into the complete coverage problem, and the final cost is the same as that of the “lawn mowing” problem [26].

IV. SENSOR-BASED COMPLETE COVERAGE PLANNING

In this section, we first discuss the SCC planner to cover the entire workspace \mathcal{W} with known target information and then generalize the algorithm to oSCC with unknown targets.

A. SCC Planner

To explain our approach, we borrow the following definitions from [19], [21]. As shown in Fig. 5(a), the *slice* is effectively a vertical line sweeping from left to right along the *sweep direction* in \mathcal{W} . A *cell* is an area where slice connectivity does not change, and changes in the connectivity of the slice only occur at *critical points*. A critical point is located on the boundary of an object whose surface normal is perpendicular to the sweep direction. Critical points are used to determine the *cell boundaries*. A *target region*, denoted by \mathcal{M}_c , is obtained by a dilated \mathbb{G}_c by a circular disk area with a radius of S . For example, \mathcal{M}_c is the yellow area in Fig. 5(a).

Unlike most MCD-based coverage path planning problems, the critical points defined here are not only on the boundary of obstacles but also on the boundary of the target regions. According to the MCD of free space \mathcal{W} , a Reeb graph [19], [21] is constructed and denoted as \mathbb{G}_w . In Fig. 5(a), $\mathbb{G}_w = (\mathcal{C}, \mathcal{E})$ is shown as the black solid lines. The nodes of \mathbb{G}_w are the critical points $\mathcal{C} = \{C_i\}$, and the edges $\mathcal{E} = \{E_i\}$ connect the neighboring critical points. The edge E_i in the Reeb graph directly corresponds to the cell \mathcal{A}_i in the free space, $i = 1, \dots, 6$, in the figure.

Algorithm 3: SCC

Input : $\mathcal{W}, \mathcal{I}, S$
Output: Path \mathcal{P}_R

- 1 $\mathbb{G}_c \leftarrow \text{Crack_Graph}(\mathcal{I})$, $(\mathcal{C}, \mathcal{E}) \leftarrow \text{MCD}(\mathcal{W} \setminus (\mathbb{G}_c \oplus S))$
- 2 $\mathbb{G}_w \leftarrow \text{Reeb_graph}(\mathcal{C}, \mathcal{E})$, $\mathcal{P}_{wc} \leftarrow \text{GCC}(\mathbb{G}_w \cup \mathbb{G}_c)$
- 3 $\text{conn} \leftarrow \text{cell_connect}(\mathcal{P}_{wc}, \mathcal{E})$
- 4 $\mathcal{P}_R \leftarrow \text{complete_coverage}(\mathcal{P}_{wc}, \mathcal{E}, \text{conn}, S)$

Algorithm 3 briefly describes the SCC planner. With \mathbb{G}_w and \mathbb{G}_c , we search the shortest cost route covering all the graph edges at least once; that is, we connect edges in both graphs to form an Euler tour with the least cost. In the case of an unspecified ending position, all of the graph nodes except for the initial and ending vertices must have an even number of connected edges (i.e., an even degree); otherwise, the robot could get stuck at vertices with odd degrees. Therefore, the degree of vertices is maintained even by adding edges. For example, as shown in Fig. 5(a), C_1 - C_6 , N_1 , and N_3 - N_5 are the vertices with odd degrees, and the red dashed edges connecting $\{C_2, N_1\}$, $\{C_3, N_3\}$, $\{C_5, N_4\}$, and $\{C_4, N_5\}$ are added to the graph to form the shortest route. The resulting Euler tour, denoted as \mathcal{P}_{wc} , provides an order of edges that the robot should visit (line 2). The connecting distance between each adjacent cell in the Euler tour is minimized in the function

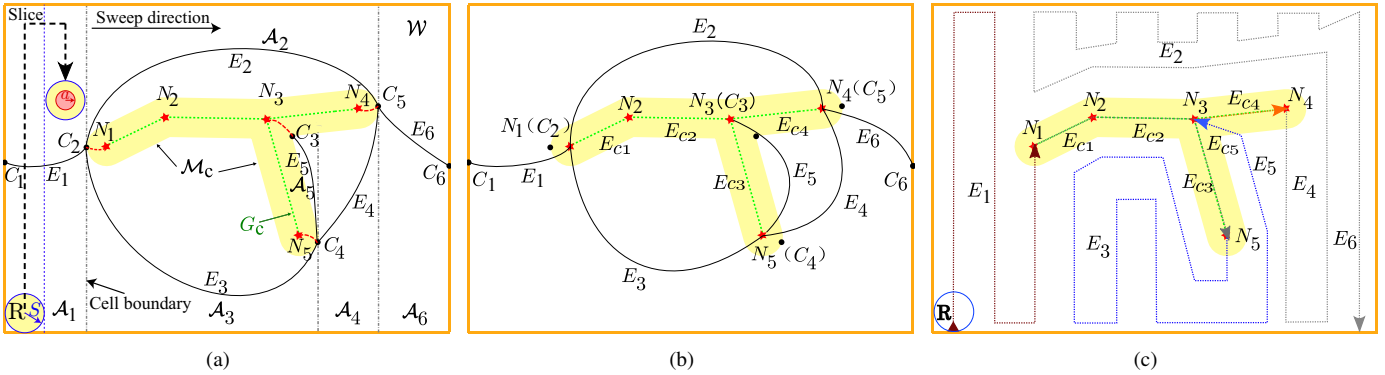


Fig. 5. Illustration of the SIFC planner. (a) The MCD with \mathcal{M}_c (highlighted in yellow). A_i , C_i , and E_i , $i = 1, \dots, 6$, represent the Reeb graph's cells, nodes, and edges, respectively. The graph \mathbb{G}_c is shown in a dotted green line, and red stars represent the nodes. The Reeb graph \mathbb{G}_w of the MCD is connected with \mathbb{G}_c . The red-dash edges are added to the combined \mathbb{G}_w and \mathbb{G}_c to form an Euler tour. (b) The simplified \mathbb{G}_w and \mathbb{G}_c . Each critical point on the boundary of the \mathcal{M}_c is combined with its corresponding node in \mathbb{G}_c . (c) The robot path \mathcal{P}_R is depicted in dotted lines, with arrows indicating the direction of travel.

`cell_connect`. The variable `conn` represents the connections of adjacent cells in the Euler tour (line 3). Finally, complete coverage is performed by following the sequence of edges in the Euler tour (line 4).

The back-and-forth motion path is generated to cover the interior of the cell sequences using the onboard sensor. Once the robot is joined with \mathbb{G}_c , it transitions to following the path \mathcal{P}_c generated by the GCC to traverse the crack graph edges, where \mathcal{P}_c is a part of \mathcal{P}_{wc} . By following the crack graph edges, the targets are covered by the robot footprint \mathcal{F} . The back-and-forth coverage motion is well documented in [19], [25]. If an edge of \mathbb{G}_w is doubled in the resulting Euler tour, the corresponding cell is split in half. The robot has the ability to adjust the height of its coverage for each slice incrementally, thereby enabling it to control the exit point of each cell [12]. Thus, by minimizing the distance from the exit to the entry points of the next cell, the connecting distance of each cell is minimized in function `cell_connect`.

As the Reeb and crack graphs provide a complete model of \mathcal{W} and each edge of the Euler tour is traversed exactly once, the proposed algorithm guarantees complete and near-optimal coverage of all the cracks and \mathcal{W} with the minimized traveling distance. The proof of the completeness and near-optimality of the SCC algorithm follows the same approach as in references [12], [42], drawing upon principles from cellular decomposition and Euler tour theory. The Reeb graph, which serves as a comprehensive model of the environment, ensures that all available free space is covered by traversing each edge exactly once. This guarantees complete coverage of all free space. The resulting Euler tour establishes a systematic order for visiting the cells of the Reeb graph without covering any area twice. While backtracking may be necessary to re-position the robot at reachable corners of the next cell to be covered, it typically adds at most one extra sweep line in length. Although some backtracking can be avoided in certain cell configurations by adjusting the order of traversal through two loops [12], even when unavoidable, the areas covered twice are usually much smaller compared to the total area. Additionally, as the environment size increases, the percentage of repeat coverage per cell decreases [42]. This ensures near-optimality. The optimal traversal ordering, equivalent to the Euler tour, can be efficiently computed in polynomial time [40].

B. oSCC Planner

When target information is unknown, robot **R** needs to detect all targets and the critical points online in \mathcal{W} . We first combine graphs \mathbb{G}_c and \mathbb{G}_w using the following lemma and propositions with proofs given in Appendices A and B.

Lemma 1: Each critical point generated by \mathcal{M}_c corresponds to one node of \mathbb{G}_c .

Proposition 1: Optimality is preserved with the choice of connecting critical points of \mathcal{M}_c to corresponding nodes in \mathbb{G}_c .

According to Proposition 1, we simplify \mathbb{G}_c and \mathbb{G}_w by combining the critical points of \mathcal{M}_c with their corresponding nodes of \mathbb{G}_c . Fig. 5(b) shows an example of the simplified graph by such action. Based on the simplified graph, we propose the oSCC planning algorithm with unknown targets. The robot first treats the target regions \mathcal{M}_c as obstacles in MCD. Then, robot **R** follows the coverage path \mathcal{P}_R until it finds those combined critical points to enter \mathcal{M}_c and follows \mathbb{G}_c according to the current Euler tour. The oSCC algorithm is a practical extension of SCC where robot **R** stores and incrementally constructs the crack graph \mathbb{G}_c online. As the robot navigates through the workspace \mathcal{W} , it continuously scans for new cracks and updates \mathbb{G}_c whenever it encounters a node (such as end points or interaction points) of the crack graph. To construct the incremental crack map, the robot utilizes existing scanned information of the crack to update the crack map, focusing only on the nodes of the cracks as shown in Algorithm 1. Subsequently, the robot enters the target region and follows the constructed crack graph until one edge ends, while simultaneously conducting footprint coverage.

Algorithm 4 shows the structure of the oSCC algorithm with three sections: initialization (lines 2 to 5), footprint coverage (lines 6 to 8), and sensing coverage (lines 9 to 11). The already footprint-covered area is denoted as \mathcal{M}_{cov} . In the initialization section, robot **R** computes Reeb graph \mathbb{G}_w for the uncovered area $\mathcal{W} \setminus \mathcal{M}_{cov}$ (line 2) without any target information \mathcal{T} . Function `Reeb_seq` computes the transverse sequence for \mathbb{G}_w using a priority queue based on the `cell` location and area, as well as the number of successive edges (children). An optimal and complete coverage path \mathcal{P}_R is generated for $\mathcal{W} \setminus \mathcal{M}_{cov}$ (line 5). In the coverage section, robot **R** follows the path calculated in the initialization section until a node of \mathbb{G}_c is encountered

(lines 9 to 11). Finally, the robot enters \mathcal{M}_c to construct \mathbb{G}_c , computes the path using the GCC planner (line 6), and follows \mathbb{G}_c until it ends (line 7). Line 8 shows the update of the covered area \mathcal{M}_{cov} . When no uncovered cells or edges remain in \mathbb{G}_w , the workspace is optimally and completely covered. An example of the robot path \mathcal{P}_R generated by Algorithm 4 is illustrated in Fig. 5(c).

Algorithm 4: oSCC

Input : $\mathcal{W}, \mathcal{I}, S$
Output: Path \mathcal{P}_R

```

1  $\mathcal{M}_{cov} \leftarrow \emptyset, \mathcal{T} \leftarrow \text{get\_topology}(\mathcal{I})$ 
  while  $\mathcal{M}_{cov} \neq \mathcal{W}$  do
2    $(\mathbf{C}, \mathbf{E}) \leftarrow \text{MCD}(\mathcal{W} \setminus \mathcal{M}_{cov})$ 
3    $\mathbb{G}_w \leftarrow \text{Reeb\_graph}(\mathbf{C}, \mathbf{E}), \mathbf{\Pi}_w \leftarrow \text{Reeb\_seq}(\mathbb{G}_w)$ 
4    $\text{conn} \leftarrow \text{cell\_connection}(\mathbf{\Pi}_w, \mathbf{E})$ 
5    $\mathcal{P}_R \leftarrow \text{complete\_coverage}(\mathbf{\Pi}_w, \mathbf{E}, \text{conn}, S)$ 
  while true do
    if A node of crack  $\mathcal{T}$  is found then
6      $\mathbb{G}_c \leftarrow \text{Crack\_Graph}(\mathcal{I}, \mathbf{\Pi}_c \leftarrow \text{GCC}(\mathbb{G}_c))$ 
7     follow_path( $\mathbf{\Pi}_c(i).nodes$ )
8      $\mathcal{M}_{cov} \leftarrow \mathcal{M}_{cov} \cup (\mathbb{G}_c \oplus S)$ 
    break
9    $P_n \leftarrow$  the next step of  $\mathcal{P}_R$ , follow_path( $P_n$ )
10   $\mathcal{M}_{cov} \leftarrow \mathcal{M}_{cov} \cup (P_n \oplus S), \mathcal{I} \leftarrow \text{get\_image}$ 
11   $\mathcal{T} \leftarrow \text{get\_topology}(\mathcal{I})$ 

```

In Algorithm 4, after traversing one target edge, the covered areas and update \mathbb{G}_w of the remaining space $\mathcal{W} \setminus \mathcal{M}_{cov}$ are removed to avoid passing the same target twice to reach another uncovered cell. Taking the example shown in Fig. 6(a), the robot is currently on node A and \mathbb{G}_w is updated after removing the already covered areas (yellow shaded areas). The odd nodes in the resulting \mathbb{G}_w include C_1, C_2, C_3 , and C_4 . Therefore, AC_2 and C_1C_3 are connected to form the least-cost Euler tour, and C_4 represents the path's ending node. When the resulting Euler tour needs to double edges in \mathbb{G}_w , the corresponding cell is split into two components. The first part is covered by a wall-following motion, where a wall is defined as the boundaries of $\mathcal{W} \setminus \mathcal{M}_{cov}$. The other part is covered by the zigzag motion of the leftover space in the cell. As shown in Fig. 6(b), edges E_1 and E_2 are doubled, and in Fig. 6(c), edges E_2 and E_3 are doubled. Note that the splitting of cells does not increase the cost of covering the whole cell. To minimize the cost, we select the coverage motion direction according to the next connected edge in the path.

We have the following property for the oSCC planner, with proof given in Appendix C.

Proposition 2: The oSCC algorithm guarantees completeness in coverage planning and results in the least-cost Euler tour for constructing the traversal ordering at the cell level, ensuring no redundancy in terms of individual cell coverage. By eliminating redundancy in individual cell coverage, it results in the most efficient path, minimizing the robot's travel distance to locally cover all the individual cells when the connections of each covered cell are not considered.

The oSCC algorithm ensures that each individual cell in the free space is covered exactly once, avoiding redundancy in terms of individual cell coverage when the connections of each covered cell are not considered. Because the dimensions of the cells are unknown, the robot does not always have enough information to minimize the zigzag motion connecting adjacent cells according to the Euler tour sequence. The optimality gap in our approach is related to the connections between adjacent cells based on the Euler tour sequence. For a worst-case analysis of the suboptimality bound, we assume that the connections between each pair of adjacent cells are small enough to be negligible in the optimal solution, and the oSCC result provides the worst connection between each pair of adjacent cells, which is the number of free cells in \mathbb{G}_w , denoted as N_{cell} , minus one (i.e., the number of connections), multiplied by $\sqrt{l^2 + (2S)^2}$ (i.e., the longest robot travel distance for one connection), where l is the slice length (the side length of the free space) and S is the sensing radius. Therefore, in the worst case, the difference from the optimal solution is bounded by $(N_{\text{cell}} - 1)\sqrt{l^2 + (2S)^2}$. The simplified \mathbb{G}_w reduces the number of edges. The algorithm is solved in polynomial time because of the structure of \mathbb{G}_w and is therefore used online efficiently.

We further illustrate the oSCC and SCC planners through an example. Fig. 6 shows the planning result under oSCC in \mathcal{W} with sizes $l = 5.79$ m and $w = 6.10$ m and robot configuration, $S = 0.69$ m and $a = 8.9$ cm. The crack information (thick dotted lines) is initially unknown. Under oSCC planner, the robot first follows the initial path planned by Algorithm 4 until detecting a crack node. Then it follows the online updated \mathbb{G}_c and uses the GCC algorithm to generate local paths for footprint coverage of the scanned cracks. The covered regions are then removed from \mathcal{W} , and \mathbb{G}_c and \mathbb{G}_w are updated accordingly. Figs. 6(a)-6(c) show the updated graphs, and Fig. 6(d) shows the final path. For comparison, Fig. 7 shows the planning results under the SCC algorithm with known crack information. The constructed MCD of the free space is shown in Fig. 7(a), along with the corresponding \mathbb{G}_w (solid lines), \mathbb{G}_c (dash lines), and \mathcal{M}_c (yellow shaded areas). The least-cost Euler tour is constructed by the blue dotted dash lines. Fig. 7(b) shows the final route of the robot. Readers can refer to the companion video clip for details. Experiments and comparisons will be further discussed in Section VII.

V. CRACK FILLING MOTION PLANNING AND CONTROL

In this section, we present the robot motion control to follow the planned trajectory and also the coordinated motion of the crack-filling action.

A. Robot Kinematic Models

Fig. 8(a) shows the bottom view of the crack-filling robot. The robot is equipped with four independently driving omnidirectional wheels, and therefore, it can move in any direction with free rotation. Fig. 8(b) illustrates the driving mechanism for the filling nozzle, denoted as \mathbf{N}_z . Two frames are used in robot modeling: a global frame $\mathcal{N}(x, y)$ and a body frame $\mathcal{B}(x_b, y_b)$. The robot footprint is assumed to be square, with

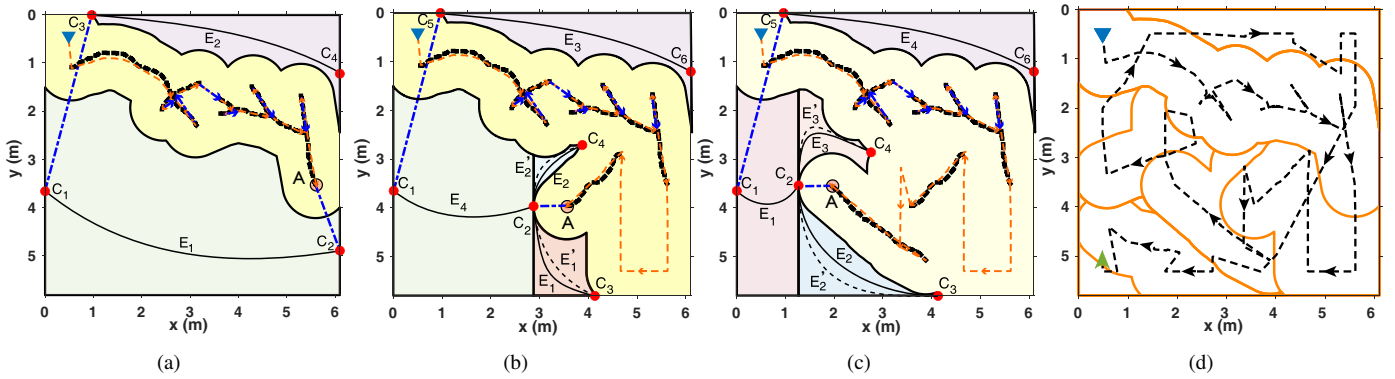


Fig. 6. An illustrative planning example by the oSCC algorithm. (a)-(c) The Reeb graphs as additional cracks are detected during the loop cycles of the oSCC algorithm. All cracks are marked by thick, dotted curves. The robot starts from the top-left corner. Each Reeb graph is updated when the robot is at point A (highlighted in a circle). Those Reeb graphs are constructed after removing already-covered areas. The red dots (C_i) denote the nodes of the Reeb graph. The solid curves (E_i) are the edges. The doubled edges are indicated by the thin, dashed black curves (E'_i). The bold boundaries are the cell boundaries. The orange-dash lines are the robot paths. The blue-dotted dashed lines are the connections between two nodes. (d) The final path using the oSCC algorithm. The final MCD of the free space is plotted in the thick orange curves. The final trajectory is shown by the black dashed lines. The robot starts from the top-left corner and ends at the bottom left, marked by a triangle and an arrow, respectively.

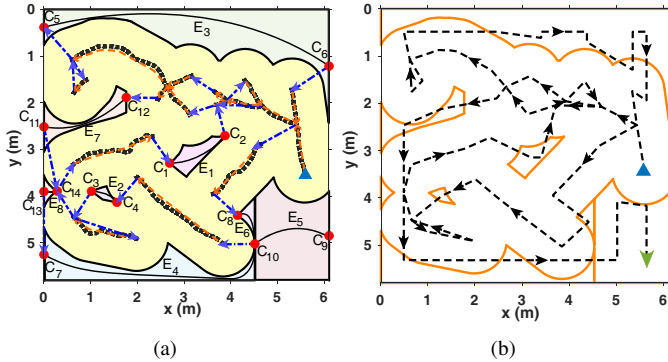


Fig. 7. Planning result by the SCC algorithm with the cracks as in Fig. 6. (a) The MCD and the corresponding G_w using SCC. The orange dotted lines are the constructed G_c . The blue-dotted dashed lines show the node connections. (b) The final route of the robot. The legends are the same as those in Fig. 6.

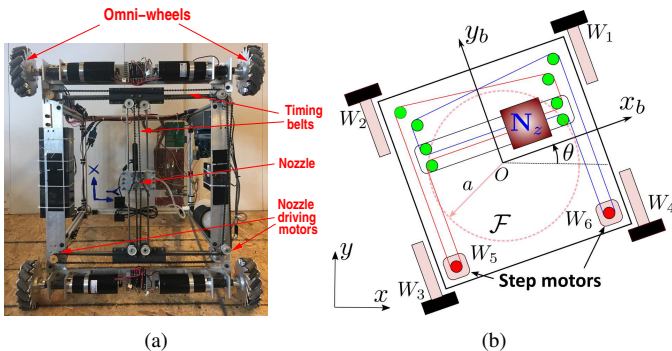


Fig. 8. (a) The bottom view of the crack-filling robot. (b) A schematic of the filling nozzle driving mechanism and robotic kinematic configuration.

its center O equidistant from four wheels, denoted by W_i , $i = 1, \dots, 4$. The distance between O and W_i is denoted as R_d . The nozzle is driven by two step motors (denoted as W_5 and W_6) with two timing belts and moves along the x_b - and y_b -axis in \mathcal{B} .

The robot pose is captured by $\mathbf{q}_r = [x_r \ y_r \ \theta]^T$ in \mathcal{N} , where (x_r, y_r) and θ are the position of robot center O and the robot orientation, respectively. The position of N_z in \mathcal{B} is denoted as $\mathbf{q}_n = [x_n \ y_n]^T$. We denote the angular velocity for W_i

as ω_i , $i = 1, \dots, 6$, and define $\boldsymbol{\omega}_r = [\omega_1 \ \omega_2 \ \omega_3 \ \omega_4]^T$ and $\boldsymbol{\omega}_n = [\omega_5 \ \omega_6]^T$. Assuming no wheel slip and no deformation of the timing belts, the kinematic models for robot motion in \mathcal{N} and nozzle relative motion in \mathcal{B} are obtained as

$$\boldsymbol{\omega}_r = \mathbf{A}_r \dot{\mathbf{q}}_r, \quad \boldsymbol{\omega}_n = \mathbf{A}_n \dot{\mathbf{q}}_n, \quad (1)$$

where

$$\mathbf{A}_r = \frac{\sqrt{2}}{R_w} \begin{bmatrix} -s_{\theta_1} & c_{\theta_1} & R_d \\ -s_{\theta_2} & c_{\theta_2} & R_d \\ -s_{\theta_3} & c_{\theta_3} & R_d \\ -s_{\theta_4} & c_{\theta_4} & R_d \end{bmatrix}, \quad \mathbf{A}_n = \frac{1}{R_g} \begin{bmatrix} 1 & -1 \\ 1 & 1 \end{bmatrix}, \quad (2)$$

R_g is the radius of the driving pulley for W_5 and W_6 , and R_w is the radius of the robot wheel. In (2), we use notations $s_\theta = \sin \theta$ and $c_\theta = \cos \theta$ for θ and other angles. Angles $\theta_1 = \theta + \pi/4$ and $\theta_{i+1} = \theta_i + \pi/2$, $i = 1, 2, 3$.

B. Filling Nozzle Motion Planning

The nozzle motion needs to be coordinated with the robot motion to efficiently fill cracks within \mathcal{F} ; see Fig. 8(b). Note that multiple cracks can be located within \mathcal{F} at a time, and we need to determine how to move the nozzle to fill these cracks while the robot is in motion. Compared to robot moving velocity, the nozzle motion in general is much faster, and therefore, for simplicity, we neglect the time duration for the nozzle to move from one crack to another (no filling action) and only count movement time along cracks (with filling action).

Fig. 9(a) illustrates the geometric relationship between robot trajectory \mathcal{P}_R and multiple cracks within \mathcal{F} . We use the arc length of path \mathcal{P}_R , denoted as s , as the parameter to characterize any arbitrary point p on cracks. For point p on a crack within \mathcal{F} , we define a projection map $\pi(p) : p \mapsto p_c(s)$, $p_c(s) \in \mathcal{P}_R$, as the minimum distance to p . Considering that n_c cracks are located within \mathcal{F} , $n_c \in \mathbb{N}$, we denote mapping $\pi_i(p)$ for the i th crack by the above definition, $i = 1, \dots, n_c$. We assume that $\pi_i(p)$ is bijective so that its inverse $\pi_i^{-1}(p)$ exists. Using $\pi_i(p)$, all points on n_c cracks inside \mathcal{F} are mapped onto \mathcal{P}_R .

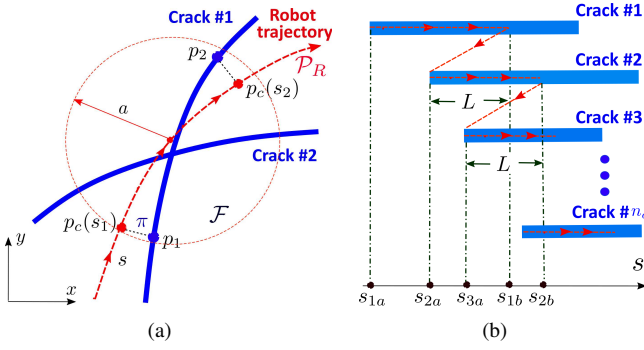


Fig. 9. (a) Schematic of the projection mapping π_i from multiple cracks to the robot path \mathcal{P}_R . (b) An illustrative example of the filling nozzle planning across multiple cracks in \mathcal{F} .

Value s increases along the robot \mathbf{R} 's moving direction, and points on n_c cracks within \mathcal{F} with the same s value have the same priority to fill. To determine the filling sequences, we consider the nozzle \mathbf{N}_z to move and switch the filling action among these n_c cracks after staying along one crack for a threshed distance L . Fig. 9(b) illustrates the nozzle travel sequence among all cracks within \mathcal{F} . Algorithm 5 describes the nozzle motion sequence planning. Input $\{\mathbf{p}_i\}_1^{n_c}$ is the point sequence sets of all cracks; that is, $\{\mathbf{p}_i\}$ contains the point sequence of the i th crack, $i = 1, \dots, n_c$. `startpoint` (line 1) is to find the first point of each crack. The function `findmin` is to find out the minimum value and the corresponding crack index. The notation $h(i)/h(I_1)$ indicates removing $h(I_1)$ from all $h(i)$ (line 3). The function `addpoint` (line 4) is to add an interval point of the crack I_1 to ${}^s\mathbf{p}_n$, and the interval is from p_1 to $p_2 + L$. Finally, we obtain the output $\{\mathbf{p}_n\}$ that represents the point sequence of the nozzle in \mathcal{B} .

Algorithm 5: Nozzle Motion Planning

Input : $\{\mathbf{p}_i\}_1^{n_c}$

Output: $\{\mathbf{p}_n\}$

- 1 $\mathbf{p}_c^i \leftarrow \pi_i(\mathbf{p}_i)$, $h(i) \leftarrow \text{startpoint}(\mathbf{p}_c^i)$, $i = 1, \dots, n_c$
 - 2 $(p_1, I_1) \leftarrow \text{findmin}(h(i))$, $m \leftarrow 0$
 - 3 **while** $m < n_c$ **do**
 - 4 $(p_2, I_2) \leftarrow \text{findmin}[h(i)/h(I_1)]$
 - 5 ${}^s\mathbf{p}_m \leftarrow \text{addpoint}(\mathbf{p}_c(I_1), p_1, p_2 + L)$
 - 6 **if** `isfinish`(I_1) **then** $m \leftarrow m + 1$, $h(I_1) \leftarrow \text{inf}$
 - 7 **else** $h(I_1) \leftarrow p_2 + L$
 - 8 $(p_1, I_1) \leftarrow (p_2, I_2)$
 - 9 $\{\mathbf{p}_n\} \leftarrow \{\pi_i^{-1}({}^s\mathbf{p}_i)\}$, $i = 1, \dots, n_c$
-

As shown in Fig. 9(b), by Algorithm 5, the first points for each crack of the first three cracks are $h(1) = s_{1a}$, $h(2) = s_{2a}$, and $h(3) = s_{3a}$. In the algorithm, $p_1 = s_{1a}$ and $I_1 = 1$ since s_{1a} is the minimum point. Then, we find the minimum from $h(2)$ and $h(3)$, so that $p_2 = s_{2a}$, $I_2 = 2$ (line 3). We also obtain $s_{1b} = s_{2a} + L$ (line 4), and therefore, all points on crack 1 from s_{1a} to s_{1b} are added to ${}^s\mathbf{p}_1$. The next iteration then adds the points on crack 2 and keeps going until all n_c cracks are covered. The value of L is chosen to provide a trade-off between the nozzle switching frequency among cracks and the

dedicating time duration to a single crack. When L is small, the switching between different cracks becomes frequent, and when L is large, it might miss filling some cracks within \mathcal{F} . We consider using $L \leq 2a$ for the switching between cracks within \mathcal{F} to have a good performance.

C. Robot and Nozzle Motion Control

The robot's orientation is independently controlled with linear velocity due to the use of omni-directional wheels. We first show the choice of orientation control. The robot driving energy expense can be represented as $J_\theta = \frac{1}{2} \sum_{i=1}^4 \omega_i^2$. Taking the derivative of J_θ over θ , we obtain

$$\frac{\partial J_\theta}{\partial \theta} = \frac{2}{R_w^2} \sum_{i=1}^4 [(\dot{x}_r^2 - \dot{y}_r^2) s_{\theta_i} c_{\theta_i} + \dot{x}_r \dot{y}_r (s_{\theta_i}^2 - c_{\theta_i}^2) - (\dot{x}_r + \dot{y}_r) R_d \dot{\theta} s_{\theta_i} + (\dot{y}_r - \dot{x}_r) R_d \dot{\theta} c_{\theta_i}]. \quad (3)$$

Using (1), it is straightforward to show that $\frac{\partial J_\theta}{\partial \theta} = 0$ and the energy expense is independent of the robot orientation. Similarly, we obtain

$$\frac{\partial J_\theta}{\partial \dot{\theta}} = \frac{2R_d}{R_w^2} \sum_{i=1}^4 [-\dot{x}_r s_{\theta_i} + \dot{y}_r c_{\theta_i} + R_d \dot{\theta}] = \frac{8R_d^2 \dot{\theta}}{R_w^2}. \quad (4)$$

The above result implies that changing the orientation increases the energy cost. Therefore, from (3) and (4), we set $\dot{\theta} = 0$ to minimize the energy expense J_θ , and in implementation, we further keep $\theta = 0$ as the desired body orientation during robot movement for simplicity.

For the robot and nozzle motion control, the objective is to reach all cracks within \mathcal{F} and complete the crack-filling action while the robot \mathbf{R} is in motion. The desired nozzle path is given by Algorithm 5 in \mathcal{B} as $\{\mathbf{p}_n\}$, while the desired robot path \mathcal{P}_R is denoted as \mathbf{p}_r in \mathcal{N} . \mathcal{P}_R is computed from the coverage path planning algorithms, specifically Algorithms 3, 4, and 6. Defining $\boldsymbol{\xi} = [\mathbf{q}_r^T \mathbf{q}_n^T]^T$ and $\mathbf{u} = [\boldsymbol{\omega}_r^T \boldsymbol{\omega}_n^T]^T$, from (1), a discrete-time state-space model is used to represent the robot and nozzle motions at the k th step

$$\boldsymbol{\xi}(k+1) = \mathbf{A}\boldsymbol{\xi}(k) + \mathbf{B}\mathbf{u}(k), \quad (5)$$

where $k \in \mathbb{N}$, $\mathbf{A} = \Delta T [(\mathbf{A}_r^T \mathbf{A}_r)^{-1} \mathbf{A}_r^T \mathbf{A}_n^{-1}]^T$ and ΔT is the sampling period.

The robot velocity is slow compared with the nozzle motion. We denote $\mathcal{X}_r \subset \mathbb{R}^3$ and $\mathcal{X}_n \subset \mathbb{R}^2$ as the allowable robot and filling nozzle velocity sets in \mathcal{N} , respectively. We then have the velocity constraints as $\|\mathbf{v}_r(k)\|_2 \leq \|\mathbf{v}_n(k)\|_2$, where $\mathbf{v}_r(k) = \dot{\mathbf{q}}_r(k) \in \mathcal{X}_r$ and $\mathbf{v}_n(k) = \dot{\mathbf{q}}_n(k) \in \mathcal{X}_n$, are the robot velocity and the nozzle relative velocity in \mathcal{N} , respectively. Using (1), \mathbf{v}_r and \mathbf{v}_n are calculated as

$$\mathbf{v}_r = (\mathbf{A}_r^T \mathbf{A}_r)^{-1} \mathbf{A}_r^T \boldsymbol{\omega}_r, \quad \mathbf{v}_n = [v_{n1} \quad v_{n2}]^T \quad (6)$$

where

$$v_{n1} = \frac{R_g}{2} (\omega_5 + \omega_6) c_\theta - {}^b x_n \dot{\theta} s_\theta + \frac{R_g}{2} (\omega_5 - \omega_6) s_\theta - {}^b y_n \dot{\theta} c_\theta + \dot{x}_r,$$

$$v_{n2} = \frac{R_g}{2} (\omega_5 + \omega_6) s_\theta + {}^b x_n \dot{\theta} c_\theta - \frac{R_g}{2} (\omega_5 - \omega_6) c_\theta - {}^b y_n \dot{\theta} s_\theta + \dot{y}_r.$$

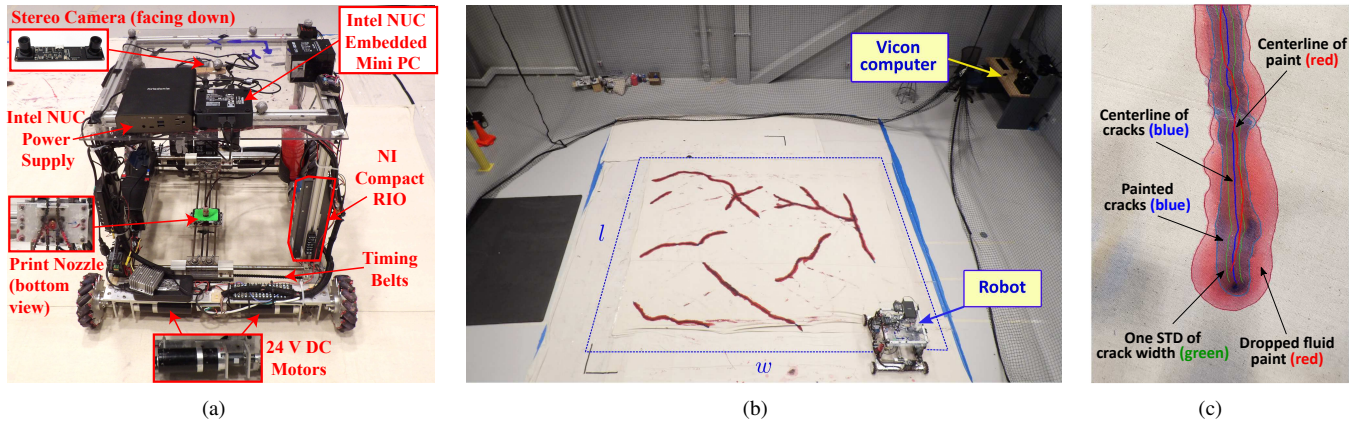


Fig. 10. (a) The omni-directional crack-filling robot with various sensors and actuators. (b) Indoor experimental setup with an optical motion capture system. (c) An illustrative example of the filling error calculation. The crack filling errors are calculated by the center-line differences between the cracks (blue) and the delivered paint (red).

Note that (6) builds the relationship between state ξ and the control input \mathbf{u} .

The objective function at the k th step is to minimize the position errors and the inputs as

$$J(k) = \sum_{i=0}^H [e_{\xi}^T(k+i)e_{\xi}(k+i) + \mathbf{u}(k+i)^T \mathbf{u}(k+i)], \quad (7)$$

where $H \in \mathbb{N}$ is the predictive horizon, error $e_{\xi}(j) = \xi(j) - \xi_d(j)$, $j \in \mathbb{N}$, desired trajectories $\xi_d = [q_{rd}^T p_n^T]^T$ and $q_{rd} = [p_r^T 0]^T$. We apply the physical constraints to keep the nozzle motion inside \mathcal{F} and motor speeds below their limits, which leads to the following MPC problem:

$$\min_{\mathbf{u}_k} J(k) \quad (8a)$$

$$\text{subj. to } \xi(k+i+1) = \xi(k+i) + \mathbf{B}\mathbf{u}(k+i), \quad (8b)$$

$$\|\mathbf{q}_n\|_2 \leq a, \|\boldsymbol{\omega}_r\| \leq \omega_r^{\max}, \|\boldsymbol{\omega}_n\| \leq \omega_n^{\max}, \quad (8c)$$

$$\|\mathbf{v}_r(k)\|_2 \leq \|\mathbf{v}_n(k)\|_2, \|\mathbf{v}_n(k)\|_2 \leq v_m, \quad (8d)$$

where $i = 0, \dots, H$, $\mathbf{u}_k = \{\mathbf{u}(k), \dots, \mathbf{u}(k+H)\}$, ω_r^{\max} , ω_n^{\max} , and v_m are the maximum velocity limits of the robot and nozzle driving motors and nozzle motion, respectively. We use YALMIP [43] to solve the MPC design in (8).

VI. EXPERIMENTAL SETUP AND EVALUATION METRICS

A. Experimental Setup

Fig. 10(a) shows the crack filling robot prototype, and Fig. 10(b) shows the indoor experimental setup. Instead of building actual cracks on the floor surface, we drew crack maps on drop cloths with blue paint to mainly test and validate the motion planner and robot control design. The robot delivered red paint to cover the drawn cracks to emulate the crack-filling action. The paint we selected for the experiments was dense, so it will not be dispensed or enlarged much after dropping on the cloth. By using such an arrangement, we can test the proposed motion planners and compare their performance with other benchmark algorithms under various crack characteristics (e.g., distribution and density) at a relatively low cost.

Using optical markers placed on the top surface of the robot and the motion capture systems (8 Vantage cameras, Vicon

Ltd.), we obtained the position and orientation of the robot at an updating frequency of 100 Hz. A hydraulic pump and a solenoid valve were used for fluid paint delivery through the nozzle. With the known robot location, the local crack images within the region centered around the robot with a range of S were fed to the planner to emulate the onboard crack detection sensor. The local position of the nozzle in the robot frame was obtained from a stereo camera mounted at the center of the robot pointing downward; see Fig. 10(a). In addition to the nozzle position, the stereo camera also provided the real-time location of the unfilled and filled cracks within \mathcal{F} .

The onboard control implementation consisted of two platforms: the low-level controller was implemented on a real-time embedded system (Compact RIO NI-cRIO-9074, National Instruments Inc.), and the upper-level controller was a portable high-performance micro-processor (Intel NUC7i7DNK, Intel Corp.). The low-level controller mainly dealt with robot motion control and crack detection and planning. The imaging processing to identify the crack positions and the stepper motor control for nozzle motion were performed on the upper-level controller. The imaging data collection and motion control were implemented at 10 Hz. Synchronization between the motion capture system and the onboard computers was implemented through a WiFi wireless connection.

As shown in Fig. 10(b), the size of the indoor testing site is $l = 5.79$ m and $w = 6.10$ m. The physical and model parameters for the robot are: $R_w = 7.6$ cm, $R_g = 1.3$ cm, $R_d = 49$ cm, $S = 69$ cm, and $a = 8.9$ cm. For the crack-filling planning and MPC design, we have the following parameters: $L = 3/5a$, $\Delta = 0.1$ s, $H = 10$, $\omega_r^{\max} = 1.31$ rad/s, $\omega_n^{\max} = 7.87$ rad/s, and $v_m = 0.1$ m/s. To create the crack maps with different densities and distributions, we used a crack image database in [44]. The density of a crack represents the Minkowski sum area of each topology (calculated by $\mathcal{T} \oplus S$) over the total workspace area. Random coordinate points and angles were generated by uniform and Gaussian distributions for the location and orientation of each topology. Four sets of crack maps were selected with different crack distributions and densities, that is, uniformly distributed cracks with a 100% density (denoted as U100) and an 80% density (U80), and Gaussian distribution cracks with a 100% density (G100) and

a 20% density (G20).

B. Evaluation Metrics

For comparison purposes, we also implemented two heuristic benchmark coverage planning algorithms. The first algorithm, denoted as ZigZag, was to generate zigzag paths using the robot footprint coverage [26]. The ZigZag method generated zigzag motion with a slice width of $2a$ (i.e., diameter of \mathcal{F}) to solve the complete footprint coverage problem. The robot followed the zigzag path and only filled the cracks under its footprint area along the path. The ZigZag algorithm presented exhaustive coverage using the robot footprint, but the coverage contained large overlap. A greedy algorithm, denoted as Greedy, was used to generate zigzag waypoints that cover the free space using the onboard detection sensor. If any targets are detected, the robot follows and covers them by footprint in the explored slices, then returns to the next unexplored waypoint to continue scanning for the targets. Algorithm 6 illustrates the implementation of the Greedy planner.

Algorithm 6: Greedy

Input : $\mathcal{W}, \mathcal{I}, S$
Output: Path \mathcal{P}_R

- 1 $\mathcal{P}_R \leftarrow \text{complete_coverage}(\mathcal{W}, S)$
- for** each unexplored waypoint of $\mathcal{P}_R \rightarrow P_n(i)$ **do**
- 2 $\text{follow_path}(P_n(i)), \mathcal{T} \leftarrow \text{get_topology}(\mathcal{I})$
- if** crack is found **then** follow \mathcal{T}

We use several metrics to evaluate the motion planning and crack-filling performance: (1) *filling time*: the total time for the nozzle to deliver paint for all cracks; (2) *robot traveling time*: the total time that the robot takes to scan and fill the cracks; (3) *robot path length* and *nozzle path length*: the total arc lengths of the robot and the nozzle traveling trajectories, respectively; (4) *sensor coverage*: the percentage of the total sensor-covered areas over the entire work space. Sensor coverage values can be greater than 100% and it quantifies the overlapped coverage ratio; and (5) *filling accuracy*: the percentage fraction of the total length of cracks with filling error that is greater than a threshold. As shown in Fig. 10(c), we calculate the crack filling error as the difference between the extracted center lines of the cracks (blue line) and the filling paint (red line). The threshold value is taken as the variation of the width of the painted marks along the crack. In this study, we calculated and used 5 mm as the threshold value.

VII. RESULTS

A. Experimental Results

We first present the experimental results under the oSCC planner and nozzle motion control. Fig. 11(a) shows the robot and nozzle motion trajectory to fill a crack map that was generated by an 80% density with a uniform distribution (i.e., U80). Under the oSCC planner, the robot started from the left-upper corner and covered the entire workspace (as the

black dash lines). The nozzle trajectory was shown as the orange lines to fill all the cracks. Fig. 11(b) further shows the robot and nozzle motion trajectories when first encountering multiple cracks within \mathcal{F} , that is, the zoom-in view of the blue boxed area shown in Fig. 11(a). The cracks and filled paint were marked by the light black and orange areas, respectively. At position N_0 , the nozzle was at the center of the robot and traveled to position N_1 where filling of the crack commenced. The nozzle completed the segment between points N_1 and N_2 . At N_2 , the nozzle motion planner worked to switch among two cracks: it filled the segment between N_2 and N_3 before switching to complete the segment between N_2 and N_4 . Filling stopped at N_4 and the nozzle then moved to position N_5 , where the segment connecting to N_6 was filled. At N_6 the nozzle completed the filling and, through the motion of the robot, moved to point N_7 . Other portions of the cracks in Fig. 11(b) that were not covered by nozzle motion from N_0 to N_7 were filled by the robot's return trajectory (as shown in Fig. 11(a)).

Fig. 11(c) plots the nozzle motion trajectory viewed in robot body frame \mathcal{B} from N_0 to N_7 . It is clear that most of the trajectories are within \mathcal{F} (marked as the red dotted circle). Note, we consider the inner circle of the rectangle robot as the footprint \mathcal{F} in the planners. The nozzle used in the experiment has the capacity to extend beyond \mathcal{F} to fill the cracks. Fig. 12 shows the robot and nozzle velocity magnitude profiles for the experiment in Fig. 11. The plots include the robot's traveling velocity magnitude (black line), the nozzle relative velocity magnitude profiles during filling cracks (thick orange dots), and no filling (orange dash lines). These results confirm the velocity constraint in (8d) that the nozzle traveling velocity during filling actuation was much larger than the robot travel velocity, while the robot moved faster when the nozzle was not in filling action. These results clearly demonstrate how the nozzle planner works together with the robot motion.

We next present the comparison results among the various coverage planning algorithms. The experiments were conducted on four crack patterns: U100, U80, G100, and G20, with four planners: oSCC, SCC, Greedy, and ZigZag. Fig. 13 shows the experimental comparison of actual crack filling outcomes. Readers can further refer to the companion video clip for experimental comparisons under the four algorithms. By experimental outcomes, all of the planners completely covered the free space and filled the cracks. The planned trajectories under oSCC and SCC were different due to the online feature of the former algorithm. The trajectories under Greedy and ZigZag shared a similar zigzag scanning pattern, but the latter generated a much denser pattern because of the smaller size of the footprint \mathcal{F} than the sensor coverage range (i.e., $a < S$).

We further conducted image processing to compute the evaluation metrics and compare the results under these planners. Table I lists the performance comparison. The GCC algorithm generates the optimal robot path for the footprint coverage problem. When the sensor range exceeds half the length of the rectangular workspace, the sensor can detect all cracks within the free space in a single scan, effectively reducing the SIFC problem to a footprint coverage problem. Therefore, the

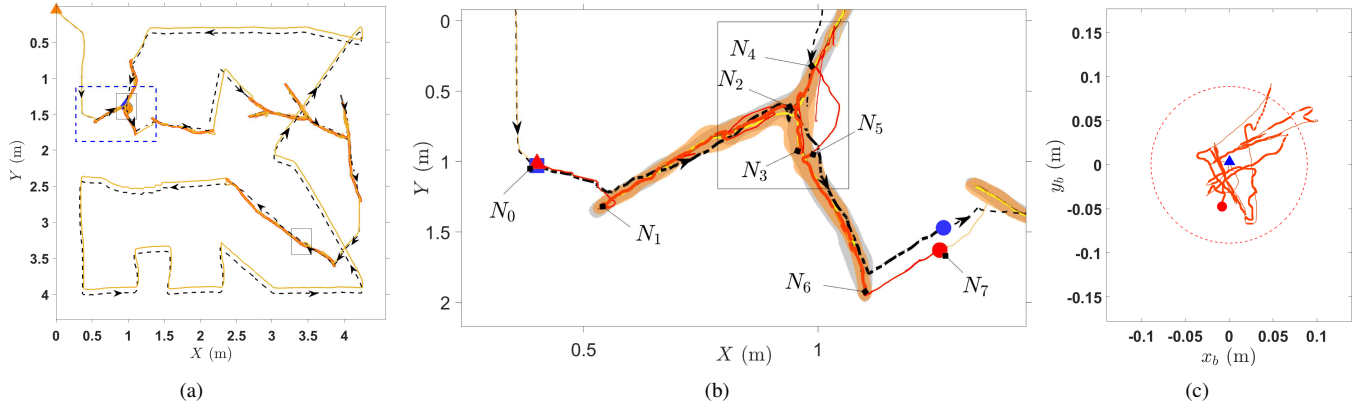


Fig. 11. Experimental results for the robot and nozzle planning and control to fill a crack map that was generated by 80% density with uniform distribution (U80). (a) Trajectories of the robot and the nozzle. The robot’s center path is represented by the dashed black curve, and the nozzle path is marked by the solid orange line. The thick orange lines indicate the painted areas. The arrows dictate the robot’s traveling direction. The orange marks “▲” and “●” indicate the robot’s starting and ending locations. (b) A zoomed-in image of the robot and nozzle path for the portion marked in the blue rectangular box in (a). The thick light-blue and orange lines indicate the cracks and painted areas, respectively. The thick and thin red line segments indicate the active (i.e., delivering paint) and inactive filling (i.e., no paint delivery) actions, respectively. The red marks “▲” and “●” indicate the nozzle’s starting and ending locations for the zoomed-in path, respectively. Similarly, the blue marks “▲” and “●” indicate the robot’s starting and ending locations for the zoomed-in path, respectively. (c) A plot of the nozzle trajectory with respect to the robot frame for the highlighted trajectory (from points N_0 to N_7) in (b). The red dotted circular region \mathcal{F} . The thick and thin line segments indicate the active and inactive filling actions. The blue mark “▲” is the starting location of the nozzle, while the red “●” indicates the nozzle’s ending location.

TABLE I
EXPERIMENT PERFORMANCE COMPARISON ON FOUR CRACK MAPS UNDER FIVE PLANNING ALGORITHMS

Crack dist.	Filling time (s)				Robot travel time (s)				Robot path length (m)				Nozzle path (m)				Sensor coverage (%)				Filling accuracy (%)			
	U100	U80	G100	G20	U100	U80	G100	G20	U100	U80	G100	G20	U100	U80	G100	G20	U100	U80	G100	G20	U100	U80	G100	G20
oSCC	731	401	356	346	1398	937	952	889	51	42	52	46	26	15	15	14	131	109	133	119	98.9	98.9	98.1	98.1
									(50)	(40)	(45)	(44)					(129)	(103)	(117)	(114)				
SCC	654	430	366	345	1328	975	919	889	51	49	49	52	23	16	14	12	132	126	127	134	99.1	99.8	98.4	98.4
									(48)	(43)	(46)	(45)					(123)	(111)	(118)	(117)				
GCC	559	364	273	276	914	577	455	455	30	19	15	13	30	20	14	12	58	34	24	20	99.1	99.8	98.4	98.4
									(29)	(17)	(13)	(12)					(60)	(34)	(24)	(20)				
Greedy	746	446	414	372	1714	1228	1104	1060	73	63	58	57	29	19	17	16	187	163	150	147	99.6	99.5	99.1	99.1
									(65)	(53)	(53)	(48)					(166)	(137)	(137)	(123)				
ZigZag	752	480	448	415	2611	2284	2149	2166	196	195	195	195	29	19	16	18	504	502	501	501	99.1	99.8	98.4	98.4
									(201)	(201)	(201)	(201)					(517)	(517)	(517)	(517)				

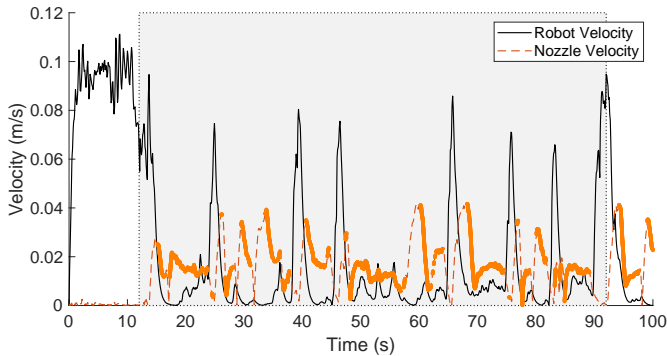


Fig. 12. Experimental results for the robot and nozzle velocities in Fig. 11. The shaded area shows the active filling region for the portion marked in the blue rectangular box in Fig. 11(a). The highlighted orange-thick segments indicate the nozzle speed when filling the cracks, and the thin orange-dash line segments indicate the inactive filling actions.

path lengths obtained from the GCC planner represent the lower bounds on the path length. For comparison purposes, the GCC

planner was also implemented and included in the table as the benchmark. In Table I, the numbers in parentheses show the simulation results under the corresponding planner. We included these simulation results to validate the computational approach. We will present additional computational results later in this section. From the evaluation metrics in Table I, we observe several facts. First, the oSCC and SCC outperformed the Greedy and ZigZag planners in terms of filling time, robot traveling time, robot path length, nozzle path length, and sensor coverage. The filling accuracy values under all planners are similar and close to 100%. Between oSCC and SCC, the performance is similar in terms of all evaluation metrics, and both are near-optimal compared with the GCC optimal planner. The sensor coverage values under all planners except GCC are more than 100%, which indicates the overlapped coverage under most planners. These comparison results confirmed that the efficiency and effectiveness of the oSCC planner achieved complete and near-optimal sensor and footprint coverage of the free space.

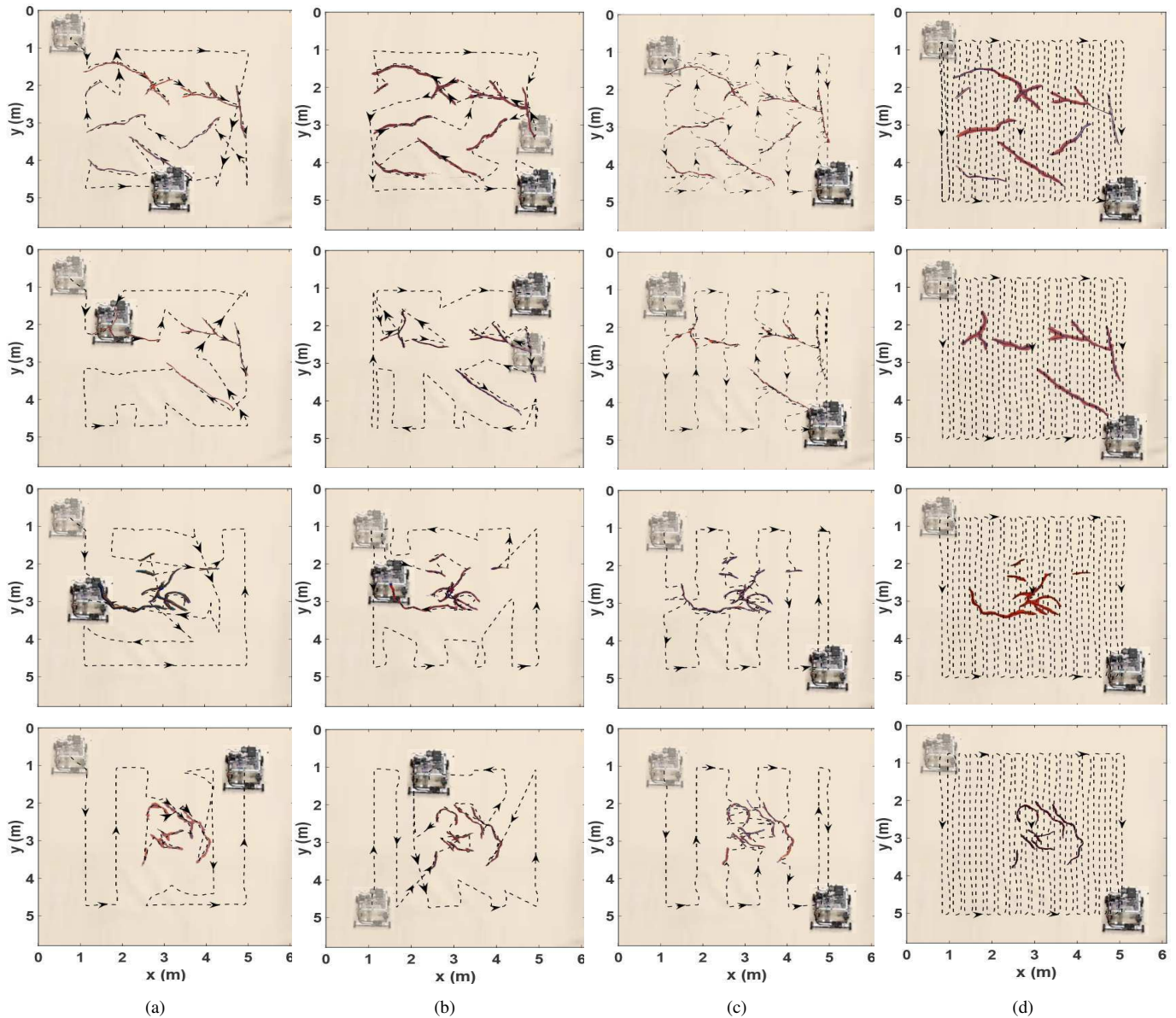


Fig. 13. The experimental comparison of crack filling outcomes with four crack density and distribution profiles. From the top to the bottom rows, the crack maps are U100, U80, G100, and G20, respectively. Each column represents the experimental results under one motion planning algorithm. The robot's starting and ending locations are marked by a "shadowed" and an actual robot image, respectively. (a) Results under the oSCC planner, (b) the SCC planner, (c) the Greedy planner, and (d) the ZigZag planner. The blue and red areas represent the cracks and red paint that were dropped by the robot to cover the cracks. The black dashed lines represent the robot center's traveling trajectories, and the arrows indicate the motion directions. More details can be found in the companion video clip.

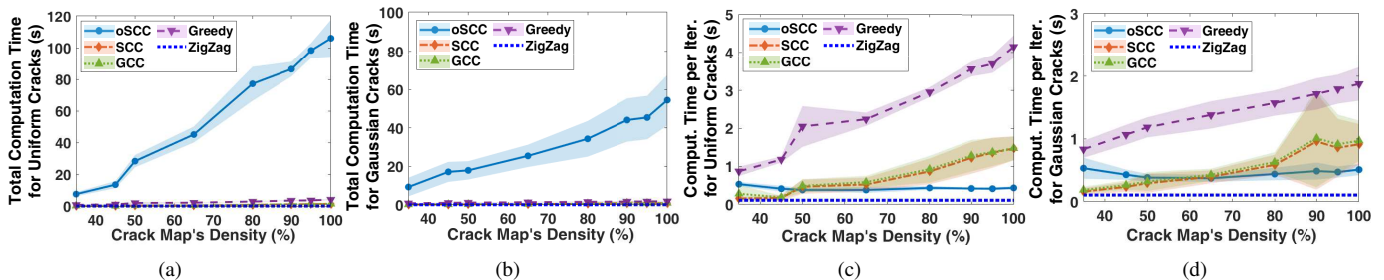


Fig. 14. Computational time comparisons of the oSCC, SCC, GCC, Greedy, and ZigZag planning algorithms for uniformly distributed cracks and Gaussian-based distributed cracks with different densities in the free space. (a) Total computation time to generate paths for uniformly distributed cracks. (b) Total computation time to generate paths for cracks with a Gaussian distribution. (c) Average computation time per iteration for cracks with uniform distribution. (d) Average computation time per iteration for Gaussian-based distributed cracks. The lines represent the mean values, while the shaded areas represent one standard deviation.

To further evaluate the algorithms, we ran simulations to obtain the statistical performance of the motion planners with different crack densities and distributions. The dimensions of the workspace and all the parameters in the simulation setup are the same as the experimental ones. By randomly selecting topology and setting centroids and the orientation of the crack points and branch angles, five sets of uniformly distributed crack maps were generated. Each set consisted of eight maps with crack densities ranging from 35% to 100%, that is, a total of $5 \times 8 = 40$ uniformly distributed crack maps. Similarly, six crack maps per density were created by generating the coordinate points with a Gaussian distribution. The center of the map was the mean, and the area in percentage was the standard deviation. To achieve a different spread of the cracks, the standard deviations were set to $\frac{1}{12}$, $\frac{1}{6}$, and $\frac{1}{3}$ of the total workspace areas. This generated a total of $6 \times 3 \times 8 = 144$ Gaussian-distributed crack maps. Therefore, a total of 184 crack maps were generated and used for testing.

We simulated and computed the performance of the oSCC, SCC, GCC, Greedy, and ZigZag planners with respect to different crack distributions (uniform and Gaussian) and densities. Figs. 14(a) and 14(b) show the total computation time comparison for the uniform and Gaussian distributions, respectively. The oSCC planner scanned and computed paths on an iterative basis, while others computed paths over the total workspace. In every iteration of the oSCC, the robot scanned the area, extracted the crack graph, and computed the shortest path. The computation time of the oSCC depended on the crack density in the workspace. From the figures, the total computation time of the oSCC planner increases linearly with crack density. The computation time difference between oSCC and SCC reflects the iterative nature of the oSCC algorithm. In terms of computation time per iteration, the oSCC matches the range of the SCC planner, as shown in Figs. 14(c) and 14(d). The oSCC has a much lower computation time per iteration than that of the Greedy planner and outperforms both the SCC and the GCC at high crack densities.

We next compared the robot path lengths and the sensor coverage against crack density. Fig. 15 shows the comparison of the robot path length and the sensor coverage for uniformly and Gaussian distributed cracks with different densities. The path lengths under the GCC and ZigZag planners are the lower and upper bounds, respectively. The statistical comparison confirms that the proposed oSCC achieves similar performance as the SCC algorithm, and both outperform the Greedy and ZigZag benchmarks. For the sensor coverage values, the oSCC, SCC, Greedy, and ZigZag planners achieve 100% workspace coverage for all the maps. The values greater than 100% measure the overlapped sensor coverage against the entire free space. Sensor overlapping shares the same trend as the path length comparison for oSCC, SCC, Greedy, and ZigZag. The overlapping area and robot path length under the Greedy algorithm are always larger than those by the oSCC. Compared to the Greedy algorithm, the oSCC planner reduces the sensor overlap by up to 62% and shortens the robot's path by up to 24% for densely and scatteredly distributed cracks. For uniformly distributed cracks, the oSCC and SCC planners achieve similar path lengths and sensor range coverage. For Gaussian-

based distributed cracks, the oSCC planner results in less sensor overlap and shorter path length than SCC. Therefore, the oSCC outperformed the other planners to cover and scan the cracks under both distributions.

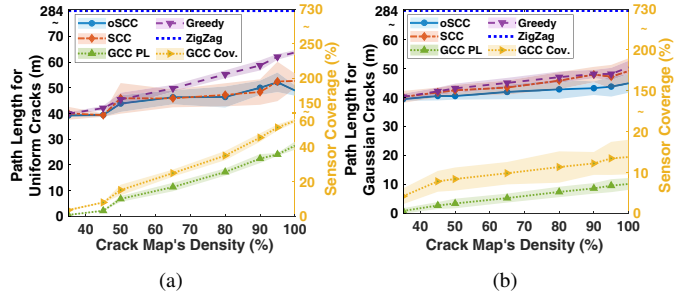


Fig. 15. Robot path length and sensor coverage comparison under the oSCC, SCC, GCC, Greedy, and ZigZag planners for (a) uniformly distributed cracks and (b) Gaussian distributed cracks with different densities. The left and right y -axis labels represent the robot path length and the sensor coverage, respectively. The orange and green dotted lines show the sensor coverage and path length for GCC, respectively. All planners except GCC achieve 100% sensor coverage. The lines and shaded areas represent the mean values and one standard deviation, respectively.

B. Discussion

To further explain the sensor overlapping results under the oSCC and SCC planners shown in Fig. 15, we look into the underlying differences in the planning algorithms. Overlapping occurs when adding minimum-cost connecting edges to the graphs to create an Eulerian graph, specifically when adding the minimum-cost path between the exit of one cell and the entry of the subsequent cell. It can also be caused by traversing an edge in the crack graph \mathbb{G}_c more than once to achieve an optimum Eulerian path. All the connecting edges account for the overlapped sensing area and the increase in path length. The oSCC planner results in less sensor overlap and shorter path length than the SCC because oSCC reduces repeated connecting edges in the online planning process, especially when the cracks are congregate. In addition, comparing Figs. 15(a) with 15(b), the sensor overlapping and the path length of the uniformly distributed cracks are larger than those of the Gaussian distribution for both the oSCC and SCC planners. These observations confirm that the connecting edges are the main contributor to sensor overlapping because the uniform distribution of cracks results in their widespread scattering, which subsequently leads to an increase in the length of the connecting edges during the LP matching process in the algorithm.

We further conducted a study to understand how the crack dispersity impacts the oSCC planner's performance. We used Gaussian distribution crack maps to illustrate the results. The crack dispersity is defined by the normal distribution of the crack centroid locations. As explained previously, three standard variations of the total workspace areas were used, namely, $\sigma_1 = \frac{1}{12}$, $\sigma_2 = \frac{1}{6}$, and $\sigma_3 = \frac{1}{3}$. Fig. 16 shows the comparison of the computation time and robot path length under the oSCC and GCC planners with varying crack density and three dispersities. We chose the GCC planner as the benchmark as discussed above. Fig. 16(a) shows the computation time (total

and per iteration) of the oSCC planner. The results show a similar trend for different crack dispersities. Fig. 16(b) presents a comparison of robot path length under three different levels of crack dispersity for both the oSCC and GCC planners. It is observed that the oSCC planner results in a reduction of robot path length when cracks are cluttered (i.e., for small values of σ). In contrast, when the crack maps are known a priori and the entire free space is not covered, the GCC planner does not exhibit a significant difference in robot path length. These observations align with the previously discussed relationship between crack dispersity and connecting edge length (i.e., the more scattered the cracks are, the longer the connecting edges), as well as the role of connecting edges between substantial cells in contributing to overlapping. The GCC planner only adds connecting edges between cracks and does not result in noticeable differences in path length for varying levels of crack dispersity. Therefore, connecting edges between substantial cells play a major role in increasing path length and overlapping.

While the robot's ability to precisely optimize the path between adjacent cells is limited due to unknown cell dimensions, extensive experimentation and comparison with GCC and SCC planners show that the final path of the oSCC planner achieves a high level of efficiency in terms of travel distance. Statistical simulations and extensive experiment results in Table I and Figs. 14-16 confirm this efficiency.

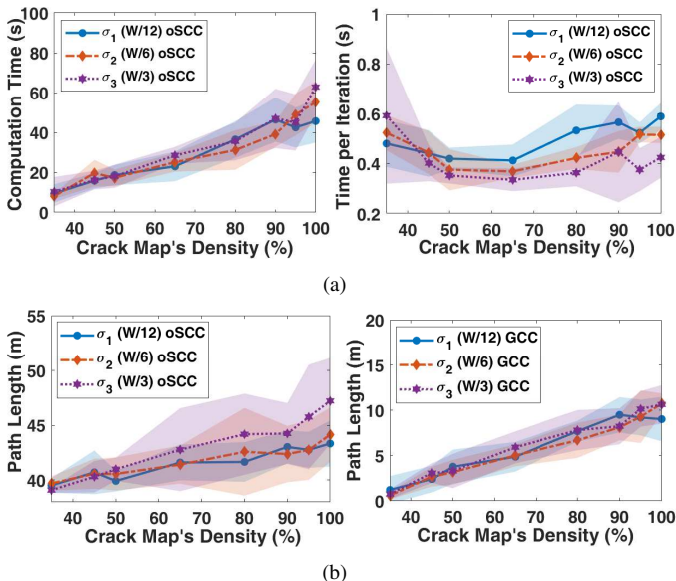


Fig. 16. Comparisons among the Gaussian maps varied by three dispersities. (a) Computation time (left) and average computation time per iteration (right) of the oSCC planner. (b) Robot path length comparison between the oSCC (left) and GCC (right) planners. The lines represent the mean values, while the shaded areas represent one standard deviation.

The robot's sensor range S and footprint radius a might vary, and those two parameters affect the Euler tour generation. We conducted simulations to analyze the robot's traveling distance under various ranges of S and a values. In experiments, the ratio between S and a is $S/a = 7.7$, and the ratio of the workspace width w to S is $w/S = 8.8$. Because the footprint size mostly influences the local path planner in the given sensor range, we therefore study the effect of varying

S when w and a are fixed. Fig. 17 shows the comparison of the robot path length over various S/a ratios under the oSCC, SCC, GCC, Greedy, and ZigZag planners for uniformly and Gaussian distributed crack maps. The path lengths under the GCC and ZigZag planners are the lower and upper bounds, respectively. When $S/a = 1$, the robot must scan the entire workspace with its footprint. Then the problem degrades into the full coverage problem, and the final path is the same as that under the ZigZag planner. When $w/S = 2$, the sensor detects all the cracks in the free space in one scan. The path lengths of oSCC and SCC converge to the results under the GCC planner. From the results in the figures, the oSCC planner outperforms the Greedy planner with different sensor ranges, particularly at large sensor ranges. When $S/a < 7$ (or $w/S > 8$), the oSCC achieves a shorter path length than SCC for uniform cracks; see Fig. 17(a). The results imply that the proposed oSCC planner yields shorter paths as the sensor range increases. This comparison provides valuable insights for the appropriate selection of planning algorithms for different applications.

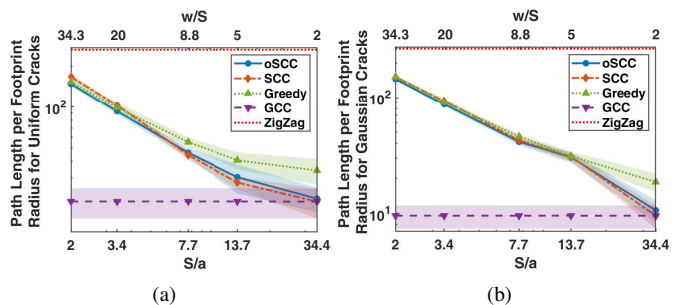


Fig. 17. Robot path length with various crack detection sensor radii (S) under the oSCC, SCC, GCC, Greedy, and ZigZag planners for (a) uniformly distributed cracks and (b) Gaussian-based distributed cracks. The workspace $w = 6.1$ m and the footprint radius $a = 8.9$ cm are fixed, and the lines and shaded areas represent the mean and one standard deviation value, respectively.

Several limitations of this work can be further explored and improved in the future. The planning algorithms assumed that the nozzle motion was fast enough such that all targets within the robot footprint \mathcal{F} could be covered in time. As a result, minimizing the robot's traveling distance was considered as the objective, and this simplified treatment decoupled the planning of robot motion from nozzle movement. The experiments were conducted in a simulated indoor environment with drop cloths and paint to create cracks and filling action, as the primary focus of the work was on the motion planning algorithm development. The performance metrics were estimated using the paint width, and even though the selected cloth did not absorb paint heavily, the results were not perfectly accurate compared to real crack-filling. We only used one mobile robot to conduct sensing and footprint coverage in this study, and it would be interesting to extend the SIFC problem with multiple collaborative robots to increase efficiency. In this work, we made assumptions about known robot locations and constant crack widths to emphasize the core planning concept and the motion planning and control algorithmic development. For future work, our focus will be on addressing uncertainties in localization by employing advanced techniques in simul-

taneous localization and mapping and achieving real-time estimation of the crack characteristics. Additionally, we plan to integrate crack width considerations into the planning algorithm’s cost and explore adaptive control algorithms to adjust the robot’s footprint coverage strategy based on encountered crack characteristics. These enhancements will significantly improve the applicability of our approach, allowing it to handle further realistic scenarios.

In this paper, we assume a known free space where the robot can move freely in any direction without obstacles. We utilize classic cell decomposition methods, specifically MCD, for both coverage tasks. The work in [19], [21] demonstrates the applicability of MCD to workspaces with various shapes and a finite number of obstacles, covering both known and unknown environments. Although obstacle handling is not the main focus of this paper, we acknowledge that in real-world situations, robot sensors can detect obstacles, and these obstacles can be geometrically represented in the environment using polygonal approximations. MCD can then incorporate the detected obstacles into the determination of cell boundaries to ensure that cells do not overlap with obstacles or cross their boundaries. The Reeb graph of the free space is constructed after cell decomposition, and it is combined with the crack graph. The robot’s motion planning algorithm, such as the oSCC planner, can generate a path to navigate through the cracks and cells while avoiding obstacles, ensuring complete coverage of the workspace. The work in [19] extended MCD into three dimensions (3D), enabling coverage of closed, orientable, and connected surfaces in 3D. While we showcase results in a known rectangular free space, the method’s adaptability permits its extension to free spaces with various shapes and even to uneven or vertical 3D surfaces, provided that the number of obstacles remains finite. This characteristic renders the method suitable for a wide range of real-world scenarios.

VIII. CONCLUSION

We have presented a motion planning and control design for simultaneous robotic sensor-based inspection and footprint coverage, with applications to crack detection and repair in civil infrastructure. To address the challenging task of simultaneously performing two complete coverage tasks in SIFC, we first proposed a graph-based target coverage algorithm for the mobile robot. Subsequently, we introduced a novel algorithm to solve the SIFC problem with unknown target information. This algorithm ensures the complete sensor scan of the workspace and the full footprint coverage of all targets, with near-optimal performance in terms of traveling distance. With the planned robot trajectory, the nozzle motion was coordinated to efficiently fill all cracks underneath the robot footprint. Extensive experimental results confirmed the effectiveness of the proposed motion planning and control algorithms under various target distributions. Furthermore, we discussed and demonstrated comparisons with other benchmark planning algorithms. The presented near-optimal and complete coverage planning algorithm has the potential to be applied to other robotic SIFC applications.

APPENDIX A SKETCH PROOF OF LEMMA 1

According to the assumption of the MCD, no two critical points change the slice connectivity at the same time. Thus, critical points that are collinear with the slice direction need special consideration. Let the endpoint node be a node with only one connected edge. With horizontal sweep direction, we treat vertical crack edges connecting with endpoint nodes as cell boundaries and those endpoint nodes as critical points, denoted as vertical critical points. For example, as shown in Fig. 18(a), N_1 , N_2 , and N_3 are vertical critical points. Since the vertical edge of the crack graph separates one cell into two adjacent cells, vertical critical points have two edges in the Reeb graph. One edge comes from the crack graph, and the other from one of the two adjacent cells. With this extension, the slice connectivity remains constant within each cell.

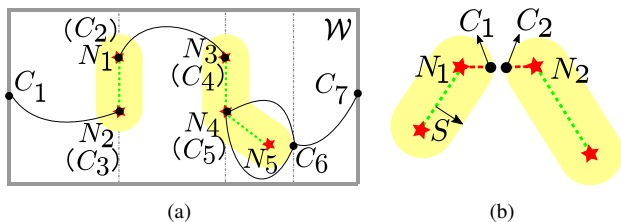


Fig. 18. (a) Special consideration is given to the vertical critical points, i.e., the endpoint nodes N_1 , N_2 , and N_3 . (b) If the distance between two critical points C_1 and C_2 is less than S , then the distance between the corresponding nodes N_1 and N_2 in the crack graph is greater than $2S$.

Except for the vertical critical points, the remaining critical points of the target region are generated by the surface normal that is perpendicular to the sweep direction. Note that the target region is the “dilated” crack graph by a circular disk with a radius of S . If the boundary of the target region is convex, we always find a node in the crack graph within an S -distance of the critical point. As shown in Fig. 5(a), critical points C_2 , C_4 , and C_5 correspond to nodes N_1 , N_5 , and N_4 in the crack graph, respectively. If the boundary of the target region is concave, then the corresponding node in the crack graph is the intersection point of edges (intersection node), e.g., critical point C_3 is associated with node N_3 in Fig. 5(a). Therefore, every critical point on the boundary of the target region is associated with one node in the crack graph. This proves the lemma.

APPENDIX B SKETCH PROOF OF PROPOSITION 1

Because of the property of the MCD, all the critical points that are generated by the convex boundaries (i.e., convex critical points) are connected to three cells. Similarly, all the critical points that are generated by the concave boundaries (i.e., concave critical points) are connected to one cell. In the Reeb graph, the convex and concave critical points correspond to nodes of degree three and one, respectively. Let us denote the convex and concave critical points of the target region as C_{vex} and C_{cav} and their corresponding crack nodes by Lemma 1 as N_{vex} and N_{cav} , respectively.

If N_{vex} is an endpoint node, then it has degree one. If N_{vex} is an intersection node, then its degree plus the number of

concave critical points associated with N_{vex} is odd. To form the Euler tour, the nodes with odd degrees need to be paired up with the least cost. Notice that the distance between C_{vex} and N_{vex} is the sensing range S . Because the distance between other nodes in the crack graph and C_{vex} is greater or equal to S , connecting each pair of C_{vex} to N_{vex} results in parts of the minimum-cost Euler tour. For the case where the distance between two critical points C_1 and C_2 is less than S , as shown in Fig. 18(b), the distance between the corresponding nodes N_1 and N_2 in the crack graph is greater than $2S$. Therefore, it is optimal to combine the C_{vex} (node of degree three) to their corresponding N_{vex} (odd degree node) in the Euler tour. Those combined nodes have an even degree, guaranteeing that the robot is not stuck at such nodes.

For C_{cav} , N_{cav} must be an intersection node. The parity of the intersection node of the crack graph is the same as the parity of the number of critical points associated with it. Therefore, pairing up these odd nodes with the least cost results in the optimal Euler tour. The vertical critical points are defined on the graph nodes by Lemma 1 and have a degree of two. The vertical critical points do not affect the optimality of the Euler tour. Thus, to find the minimum cost of the Euler tour, the edge of the crack graph never gets doubled, as all the critical points of the target region result in even degrees by connecting them to their corresponding nodes in the crack graph. To pair up other odd nodes in the Reeb graph, only edges corresponding to the cells (free space) get doubled. Doubling the selected edges means splitting the corresponding cells into two portions, which does not increase the cost of covering the whole area. Thus, as all parts of the free space and crack graph are covered exactly once, optimality is preserved. This proves the proposition.

APPENDIX C SKETCH PROOF OF PROPOSITION 2

The completeness of the oSCC planner follows directly from the properties of the Euler tour used to solve the route. By definition, the construction of \mathbb{G}_w does not stop until all the areas in \mathcal{W} are covered. The Reeb graph \mathbb{G}_w provides a complete representation of the free space. Because each edge of the graph is traversed (i.e., each cell is covered), it guarantees that all available free spaces are covered. Therefore, the algorithm is complete.

The oSCC planner reinforces the connections of the critical points to their corresponding nodes in \mathbb{G}_c until reaching its end. The resulting least-cost Euler tour, obtained from the doubling of selected edges, establishes an order in which the cells of the Reeb graph should be visited. The Euler tour ensures that no area is covered twice by not traversing any edge twice. Note that the covered spaces are removed from \mathcal{W} , and the cell coverage does not duplicate any covered area. Doubling the edges of cells does not increase any cost because the two cell components do not overlap. By definition, no edge of the Euler tour is traversed twice, and this implies no area is covered twice. Therefore, the algorithm ensures no redundancy in terms of individual cell coverage, as all free space is covered exactly once from the least-cost Euler tour, resulting in the most efficient path that minimizes the robot's travel distance

to locally cover all the individual cells when the connections of each covered cell are not considered.

REFERENCES

- [1] J. Zhang, X. Yang, W. Wang, J. Guan, L. Ding, and V. C. Lee, "Automated guided vehicles and autonomous mobile robots for recognition and tracking in civil engineering," *Automat. Constr.*, vol. 146, p. 104699, 2023.
- [2] M. Eskandari Torbaghan, B. Kaddouh, M. Abdellatif, N. Metje, J. Liu, R. Jackson, C. D. Rogers, D. N. Chapman, R. Fuentes, M. Miodownik *et al.*, "Robotic and autonomous systems for road asset management: a position paper," *Proc. Inst. Civ. Eng., Smart Infrastruct. Constr.*, vol. 172, no. 2, pp. 83–93, 2020.
- [3] H. M. La, R. S. Lim, B. B. Basily, N. Gucunski, J. Yi, A. Maher, F. A. Romero, and H. Parvardeh, "Mechatronic systems design for an autonomous robotic system for high-efficiency bridge deck inspection and evaluation," *IEEE/ASME Trans. Mechatronics*, vol. 18, no. 6, pp. 1655–1664, 2013.
- [4] H. La, R. Lim, B. Basily, N. Gucunski, J. Yi, A. Maher, F. Romero, and H. Parvardeh, "Autonomous robotic system for high-efficiency non-destructive bridge deck inspection and evaluation," in *Proc. IEEE Conf. Automat. Sci. Eng.*, Madison, WI, 2013, pp. 1065–1070.
- [5] N. Gucunski, B. Basily, J. Kim, J. Yi, T. Duong, K. Dinh, S.-H. Kee, and A. Maher, "RABIT: implementation, performance validation and integration with other robotic platforms for improved management of bridge decks," *Int. J. Intell. Robot. Appl.*, vol. 1, no. 3, pp. 271–286, 2017.
- [6] R. Bormann, F. Jordan, J. Hampp, and M. Hägele, "Indoor coverage path planning: Survey, implementation, analysis," in *Proc. IEEE Int. Conf. Robot. Autom.*, 2018, pp. 1718–1725.
- [7] X. Kan, H. Teng, and K. Karydis, "Online exploration and coverage planning in unknown obstacle-cluttered environments," *IEEE Robot. Autom. Lett.*, vol. 5, no. 4, pp. 5969–5976, 2020.
- [8] C. Wu, C. Dai, X. Gong, Y.-J. Liu, J. Wang, X. D. Gu, and C. C. Wang, "Energy-efficient coverage path planning for general terrain surfaces," *IEEE Robot. Autom. Lett.*, vol. 4, no. 3, pp. 2584–2591, 2019.
- [9] A. T. Palacios, A. Sánchez L, and J. M. E. Bedolla Cordero, "The random exploration graph for optimal exploration of unknown environments," *Int. J. Adv. Robot. Syst.*, vol. 14, no. 1, 2017, article 1729881416687110.
- [10] E. Galceran and M. Carreras, "A survey on coverage path planning for robotics," *Robot. Auton. Syst.*, vol. 61, no. 12, pp. 1258–1276, 2013.
- [11] C. S. Tan, R. Mohd-Mokhtar, and M. R. Arshad, "A comprehensive review of coverage path planning in robotics using classical and heuristic algorithms," *IEEE Access*, vol. 9, pp. 119 310–119 342, 2021.
- [12] R. Mannadiar and I. Rekleitis, "Optimal coverage of a known arbitrary environment," in *Proc. IEEE Int. Conf. Robot. Autom.*, Anchorage, AK, 2010, pp. 5525–5530.
- [13] I. Rekleitis, A. P. New, E. S. Rankin, and H. Choset, "Efficient boustrophedon multi-robot coverage: an algorithmic approach," *Ann. Math. Artif. Intell.*, vol. 52, no. 2, pp. 109–142, 2008.
- [14] J. Song and S. Gupta, "ε*: An online coverage path planning algorithm," *IEEE Trans. Robotics*, vol. 34, no. 2, pp. 526–533, 2018.
- [15] —, "Care: Cooperative autonomy for resilience and efficiency of robot teams for complete coverage of unknown environments under robot failures," *Auton. Robots*, vol. 44, no. 3, pp. 647–671, 2020.
- [16] H. ElGibreen and K. Youcef-Toumi, "Dynamic task allocation in an uncertain environment with heterogeneous multi-agents," *Auton. Robots*, vol. 43, no. 7, pp. 1639–1664, 2019.
- [17] E. Gonzalez, O. Alvarez, Y. Diaz, C. Parra, and C. Bustacara, "Bsa: A complete coverage algorithm," in *Proc. IEEE Int. Conf. Robot. Autom.*, Barcelona, Spain, 2005, pp. 2040–2044.
- [18] J. Tang, C. Sun, and X. Zhang, "Mstc*: multi-robot coverage path planning under physical constrain," in *Proc. IEEE Int. Conf. Robot. Autom.*, Xi'an, China, 2021, pp. 2518–2524.
- [19] E. U. Acar, H. Choset, A. A. Rizzi, P. N. Atkar, and D. Hull, "Morse decompositions for coverage tasks," *Int. J. Robot. Res.*, vol. 21, no. 4, pp. 331–344, 2002.
- [20] H. Choset and P. Pignon, "Coverage path planning: The boustrophedon cellular decomposition," in *Proc. Int. Conf. on Field and Service Robotics*, Canberra, Australia, 1998, pp. 203–209.
- [21] E. U. Acar and H. Choset, "Sensor-based coverage of unknown environments: Incremental construction of morse decompositions," *Int. J. Robot. Res.*, vol. 21, no. 4, pp. 345–366, 2002.

- [22] E. U. Acar, H. Choset, and J. Y. Lee, "Sensor-based coverage with extended range detectors," *IEEE Trans. Robotics*, vol. 22, no. 1, pp. 189–198, 2006.
- [23] E. Acar, H. Choset, Y. Zhang, and M. Schervish, "Path planning for robotic demining: robust sensor-based coverage of unstructured environments and probabilistic methods," *Int. J. Robot. Res.*, vol. 22, no. 7-8, pp. 441–466, 2003.
- [24] Y. Gabriely and E. Rimon, "Spiral-stc: An on-line coverage algorithm of grid environments by a mobile robot," in *Proc. IEEE Int. Conf. Robot. Autom.*, Philadelphia, PA, 2002, pp. 954–960.
- [25] H. Choset, "Coverage for robotics—a survey of recent results," *Ann. Math. Artif. Intell.*, vol. 31, no. 1-4, pp. 113–126, 2001.
- [26] S. LaValle, *Planning Algorithms*. New York, NY: Cambridge University Press, 2006.
- [27] T. Ersson and X. Hu, "Path planning and navigation of mobile robots in unknown environments," in *Proc. IEEE/RSJ Int. Conf. Intell. Robot. Syst.*, Maui, HI, 2001, pp. 858–864.
- [28] M. Likhachev, D. I. Ferguson, G. J. Gordon, A. Stentz, and S. Thrun, "Anytime dynamic A*: An anytime, replanning algorithm," in *Proc. Int. Conf. Automated Plan. Sched.*, 2005, pp. 262–271.
- [29] L. Paull, S. Saeedi, M. Seto, and H. Li, "Sensor-driven online coverage planning for autonomous underwater vehicles," *IEEE/ASME Trans. Mechatronics*, vol. 18, no. 6, pp. 1827–1838, 2013.
- [30] J. Hess, M. Beinhofer, D. Kuhner, P. Ruchti, and W. Burgard, "Poisson-driven dirt maps for efficient robot cleaning," in *Proc. IEEE Int. Conf. Robot. Autom.*, 2013, pp. 2245–2250.
- [31] J. Hess, M. Beinhofer, and W. Burgard, "A probabilistic approach to high-confidence cleaning guarantees for low-cost cleaning robots," in *Proc. IEEE Int. Conf. Robot. Autom.*, Hong Kong, China, 2014, pp. 5600–5605.
- [32] N. Rottmann, R. Denz, R. Bruder, and E. Rueckert, "A probabilistic approach for complete coverage path planning with low-cost systems," in "Proc. 2021 Europ. Conf. Mobile Robots, Bonn, Germany, 2021, pp. 1–8.
- [33] Y. Liu, J. J. Zhu, R. L. Williams, and J. Wu, "Omni-directional mobile robot controller based on trajectory linearization," *Robot. Auton. Syst.*, vol. 56, no. 5, pp. 461–479, 2008.
- [34] G. Indiveri, "Swedish wheeled omnidirectional mobile robots: Kinematics analysis and control," *IEEE Trans. Robotics*, vol. 25, no. 1, pp. 164–171, 2009.
- [35] K. Yu, C. Guo, and J. Yi, "Complete and near-optimal path planning for simultaneous sensor-based inspection and footprint coverage in robotic crack filling," in *Proc. IEEE Int. Conf. Robot. Autom.*, Montreal, Canada, 2019, pp. 8812–8818.
- [36] C. Guo, K. Yu, Y. Gong, and J. Yi, "Optimal motion planning and control of a crack filling robot for civil infrastructure automation," in *Proc. IEEE Conf. Automat. Sci. Eng.*, Xi'an, China, 2017, pp. 1463–1468.
- [37] M.-K. Kwan, "Graphic programming using odd or even points," *Chinese Math*, vol. 1, pp. 273–277, 1962.
- [38] N. Christofides, V. Campos, A. Corberán, and E. Mota, "An algorithm for the rural postman problem," Imperial College London, London, UK, Report IC.O.R.81.5, 1981.
- [39] W. L. Pearn and T. Wu, "Algorithms for the rural postman problem," *Comput. Oper. Res.*, vol. 22, no. 8, pp. 819–828, 1995.
- [40] J. Edmonds and E. L. Johnson, "Matching, euler tours and the chinese postman," *Math. Program.*, vol. 5, no. 1, pp. 88–124, 1973.
- [41] M. Fleury, "Deux problemes de geometrie de situation," *J. de Mathematiques Element. 2nd ser. (in French)*, vol. 2, pp. 257–261, 1883.
- [42] A. Xu, C. Viriyasuthee, and I. Rekleitis, "Efficient complete coverage of a known arbitrary environment with applications to aerial operations," *Auton. Robots*, vol. 36, pp. 365–381, 2014.
- [43] J. Löfberg, "YALMIP : A toolbox for modeling and optimization in MATLAB," in *Proc. 2004 IEEE Int. Symp. Comp. Aided Control Syst. Design*, Taipei, Taiwan, 2004, pp. 284–289.
- [44] Y. Shi, L. Cui, Z. Qi, F. Meng, and Z. Chen, "Automatic road crack detection using random structured forests," *IEEE Trans. Intell. Transport. Syst.*, vol. 17, no. 12, pp. 3434–3445, 2016.